

1 **Relative importance of the mechanisms triggering the Eurasian** 2 **ice sheet deglaciation in the GRISLI2.0 ice sheet model**

3 **Victor van Aalderen¹, Sylvie Charbit¹, Christophe Dumas¹, and Aurélien Quiquet¹**

4 ¹Laboratoire des Sciences du Climat et de l'Environnement, LSCE/IPSL, CEA-CNRS-UVSQ, Université Paris-
5 Saclay, 91191 Gif-sur-Yvette cedex, France

6 **Corresponding author:** Victor van Aalderen (victor.van-aalderen@lsce.ipsl.fr)

7 **Abstract**

8 The last deglaciation (21000 to 8000 years BP) of the Eurasian ice sheet (EIS), is thought to have been responsible
9 for a sea level rise of about 20 meters. While many studies have examined the timing and rate of the EIS retreat
10 during this period, many questions remain about the key processes that triggered the EIS deglaciation 21,000 years
11 ago. Due to its large marine-based parts in the Barents-Kara and British Isles sectors, BKIS is often considered as
12 a potential analog of the current West Antarctic ice sheet (WAIS). Identifying the mechanisms that drove the EIS
13 evolution might provide a better understanding of the processes at play in the West Antarctic destabilization. To
14 investigate the relative impact of key drivers on the EIS destabilization we used the three-dimensional ice sheet
15 model GRISLI (version 2.0) forced by climatic fields from five PMIP3/PMIP4 LGM simulations. In this study,
16 we performed sensitivity experiments to test the response of the simulated Eurasian ice sheets to surface climate,
17 oceanic temperatures (and thus basal melting under floating ice tongues) and sea level perturbations. Our results
18 highlight that the EIS retreat simulated with the GRISLI model is primarily triggered by atmospheric warming.
19 Increased atmospheric temperatures further amplify the sensitivity of the ice sheets to sub-shelf melting. These
20 results contradict those of previous modelling studies mentioning the central role of basal melting on the
21 deglaciation of the marine-based Barents-Kara ice sheet. However, we argue that the differences with previous
22 works are mainly related to differences in the methodology followed to generate the initial LGM ice sheet. Due to
23 the strong sensitivity of EIS to the atmospheric forcing highlighted with the GRISLI model and the limited extent
24 of the confined ice shelves during the LGM, we conclude by questioning the analogy between EIS and the current
25 WAIS. However, because of the expected rise in atmospheric temperatures, risk of hydrofracturing is increasing
26 and could ultimately put the WAIS in a configuration similar to the past Eurasian ice sheet.

27

28

29

30

31

32

33

34 **1 Introduction**

35 During the last glacial maximum (LGM, 26-19 ka), the Eurasian ice complex was formed by the coalescence of
36 three distinct ice sheets covering the British Isles, Fennoscandia and the Barents and Kara Seas. While the
37 Fennoscandian ice sheet (FIS) was mostly grounded on the bedrock, the British Isles (BIIS) and Barents-Kara
38 (BKIS) were mostly lying below sea level.

39 The Eurasian ice sheet (EIS) was influenced by various climate regimes with large differences between the western
40 and eastern edges. Due to heat and moisture sources from the North Atlantic current, the British Isles and western
41 Scandinavia were dominated by relatively warm and wet conditions contrasting with the more continental and
42 drier climate in the eastern part of the EIS (Tierney et al., 2020). These various climatic influences prevailing over
43 the three different ice sheets forming the Eurasian ice complex, may have resulted in different responses to
44 variations in atmospheric and oceanic conditions. Over the last decade an active field of research has developed to
45 identify the mechanisms behind the retreat of the Eurasian ice sheet during the last deglaciation, although no clear
46 consensus has yet been reached. According to the recent study of Sejrup et al. (2022) the onset of the northern
47 hemisphere deglaciation was primarily triggered by summer ablation resulting from increased summer insolation
48 at 65 °N, and thus by changes in surface mass balance (SMB), defined as the difference between snow/ice
49 accumulation and ablation.

50 On the other hand, studies based on modeling approaches suggest that the retreat of marine-based ice sheets could
51 be driven by dynamical processes triggered by the melting of ice shelves (Pattyn et al., 2018). In fact, the
52 relationship between oceanic temperatures and ice sheet mass balance has been confirmed and widely documented
53 for the present-day WAIS. In particular, it has been shown that ocean warming plays a crucial role in accelerating
54 Antarctic mass loss by enhancing basal melting and ice shelf thinning (Pritchard et al., 2012, Konrad et al., 2018,
55 Pattyn et al., 2018; Rignot et al., 2019). This process may trigger a marine ice sheet instability when the bedrock
56 is sloping towards the ice sheet interior. This instability translates into a sustained retreat of the grounding line and
57 a significant glacier acceleration (Schoof, 2012). As large parts of BIIS and BKIS are marine based, their evolution
58 could be driven by sub-shelf melting and potentially by the subsequent marine ice sheet instability. Based on the
59 analysis of benthic and planktic foraminiferal assemblages, ice-rafted debris and radiocarbon dating, Rasmussen
60 and Thomsen (2021) showed that the retreat of the ice in the Svalbard-Barents sector followed the deglacial
61 oceanic, but also atmospheric, temperature changes. Relying on a first-order thermomechanical ice sheet model
62 constrained by a variety of geomorphological, geophysical and geochronological data, Patton et al. (2017) found
63 that the BIIS receded quite quickly in response to moderate increases in surface temperature. By contrast, the BKIS
64 was rather affected by a combination of reduced precipitation and increased rates of iceberg calving. Other
65 modeling studies have attempted to simulate the dynamics of the EIS during the last glacial period and the last
66 deglaciation with the objective of better understanding the evolution of the ice sheet (Petrini et al., 2020; Alvarez-
67 Solas et al., 2019). In a way similar to what is currently observed in West Antarctica, they suggest that large EIS
68 variations are primarily due to the warming of the Atlantic Ocean leading to increased basal melting in the vicinity
69 of the grounding line (Petrini et al., 2020; Alvarez-Solas et al., 2019). However, the models on which these studies
70 are based have no specific treatment for computing ice velocities at the grounding line, making questionable their
71 representation of the grounding line migration.

72 Because of the diversity of mechanisms that may have influenced the evolution of the three Eurasian ice sheets,
73 the Eurasian ice complex is an interesting case study to investigate the different mechanisms responsible for the
74 ice sheet retreat. As both BKIS and BIIS are marine-based (Svendsen et al., 2004, Gandy et al., 2018, 2021), they
75 are likely to be more sensitive to oceanic temperature variations. Special attention can be given to BKIS because
76 it has often been considered as a potential analogue of the present-day WAIS (Gudlaugsson et al., 2017,
77 Andreassen and Winsborrow, 2009, Mercer, 1970) due to common features such as the ice volume and a bedrock
78 largely grounded below sea level with an upstream deepening (Amante et al., 2009). As a result, in-depth
79 investigations of the BKIS behavior at the LGM can help to better understand the present-day changes and future
80 evolution of West Antarctica.

81 This wide range of hypotheses regarding the different processes responsible for the EIS destabilization (i.e.
82 atmospheric climate, oceanic climate or both) confirms that there is still a lot of unknowns in the EIS dynamics
83 during the last deglaciation and that the debate is not closed. Progress has been made in ice sheet modeling with
84 the development of new generation models computing the full Stocks flow equations. For example, with a refined
85 model resolution near the grounding line, Gandy et al., (2018, 2021) have quantified the impact of oceanic
86 temperatures on the grounding line dynamics and investigated the potential occurrence and effect of the marine
87 ice sheet instability. However, as the computation time is considerably increased, they focus only on specific
88 sectors (i.e. North Sea) and thus do not consider the impact of the other interconnected ice sheets.

89 In this paper, we present simulations of the entire Eurasian ice complex during the LGM using the three-
90 dimensional GRISLI2.0 (GRenoble Ice Shelf and Land Ice) ice sheet model (Quiquet et al., 2018). GRISLI2.0
91 includes an explicit calculation of the ice flux at the grounding line derived from the analytical formulation
92 provided by Tsai et al. (2015), which is expected to account for the representation of the marine ice sheet instability.
93 Our ultimate objective is not to reproduce the exact timing of the last deglaciation of the EIS but rather to explore
94 the sensitivity of EIS to various perturbations using the GRISLI ice model.

95 Starting from its LGM geometry, we investigate the EIS sensitivity to perturbations of surface air temperature,
96 precipitation rate, basal melting, and sea level to better understand their relative contribution to the EIS
97 destabilization. In this work, the GRISLI2.0 ice sheet model was forced by a panel of ten different climates from
98 the Paleoclimate Modelling Intercomparison Project (PMIP) database (Abe-Ouchi et al., 2015; Kageyama et al.,
99 2021).

100 The paper is organized as follows. Section 2 provides a description of the basic equations of the GRISLI2.0 ice
101 sheet model. It also includes a presentation of the climate forcing and the experimental setup of the LGM and
102 sensitivity experiments. Section 3 compares our different reconstructions of the EIS at the LGM. The results of
103 the sensitivity experiments are presented in section 4 and discussed in section 5. Concluding remarks are given in
104 section 6.

105



106

107 **Figure 1:** Map of the Eurasian Ice Sheet at the LGM. The white line is the most credible ice extent of the Eurasian
 108 ice sheet at the LGM according to the DATED-1 compilation (Hughes et al., 2016). Dark blue shaded areas
 109 correspond to the location of the main ice streams (Dowdeswell et al., 2016; Stokes and Clark, 2001), and dotted
 110 black lines are delimitations between the Fennoscandian, the Barents-Kara, and the British Isles ice sheets.

111 **2. Model description and experimental set-up**

112 **2.1 The GRISLI ice sheet model**

113 In this study, we use the 3D thermomechanical ice sheet model GRISLI2.0 (referred hereafter to as GRISLI) run
 114 on a Cartesian grid with a horizontal resolution of 20 km x 20 km, corresponding to 177 x 257 grid points.

115 This ice sheet model was initially built to study the Antarctic ice sheet behavior during glacial-interglacial cycles
 116 (Ritz et al. 2001). It was then adapted to the Northern Hemisphere ice sheets (e.g. Peyaud et al., 2007) and tested
 117 under various climatic conditions (Ladant et al., 2014, Le clec'h et al. 2019, Colleoni et al., 2014, Beghin et al.
 118 2014). GRISLI also took part in the Ice Sheet Model Intercomparison Project (ISMIP6) (Goelzer et al.; 2020,
 119 Seroussi et al., 2020, Quiquet and Dumas, 2021a, 2021b) to investigate future sea level changes (Nowicki et al.
 120 2020). A full description of GRISLI can be found in Quiquet et al. (2018). Here, we only remind the basic
 121 principles of the model. The main modification in this new version of GRISLI compared to previous ones (Ritz et

122 al., 2001; Peyaud et al., 2007) is the implementation of analytical formulations of the flux at the grounding line
123 leading to a better representation of the grounding line migration.

124 The evolution of the ice sheet geometry depends on the ice sheet surface mass balance, ice dynamics and isostatic
125 adjustment. Assuming that ice is an incompressible material, changes in ice thickness with time are given by the
126 mass balance equation:

$$127 \quad \frac{dH}{dt} = SMB - B_{melt} - \nabla(UH) \quad (1)$$

128 with H being the local ice thickness, SMB the surface mass balance, B_{melt} the basal melting in grounded ice areas
129 and under the ice shelves, U the vertical average velocity, and $\nabla(UH)$ the ice flux divergence.

130 The ice velocity is calculated from the sum of the shallow ice approximation (SIA) and the shallow shelf
131 approximation (SSA) components (Winkelmann et al., 2011). Both approximations take advantage of the small
132 aspect ratio of the ice sheets (Hutter, 1983). The SIA assumes that the longitudinal shear stresses can be neglected
133 compared to the vertical shear stresses and holds for all ice sheet regions where the gravity-driven flow induces a
134 slow motion of the ice (Hutter, 1983). Conversely, the SSA neglects the vertical shear stresses compared to the
135 longitudinal shear stresses, which is generally valid for floating ice shelves (MacAyeal, 1989) and to some extent
136 for fast-flowing ice streams. As a result, the total ice sheet domain can be separated into three regions: floating ice
137 shelves where the ice velocity is computed with the SSA, cold-base areas governed by the SIA, and finally, the
138 temperate-base grounded ice, where the ice velocity is computed as the sum of the SIA and SSA components.

139 The basal friction for the temperate base areas is assumed to follow a linear friction law:

$$140 \quad \tau_b = -\beta U_b \quad (2)$$

141 where τ_b is the basal shear stress, U_b the basal velocity and β the basal drag coefficient. The basal drag coefficient
142 depends on the effective water pressure (N), i.e. the difference between water pressure and ice pressure, and on an
143 internal constant parameter ($C_f = 1.5 \cdot 10^{-6} \text{ m yr}^{-1}$):

$$144 \quad \beta = C_f N \quad (3)$$

145 The effective pressure N depends on the groundwater hydrology which is calculated according to Darcy's law
146 (Quiquet et al., 2018).

147 At the base of the grounded ice sheet, the basal temperature is also critically dependent on the geothermal heat
148 flux which is given here by the distribution of Shapiro and Ritzwoller (2004).

149 To simulate artificially the effect of ice anisotropy on the ice velocity, most ice sheet models use an enhancement
150 factor in the non-linear viscous flow law that relates deformation rates and stresses with values generally ranging
151 between 1 and 5. In GRISLI, two enhancement factors are considered (E_{SIA} and E_{SSA}). E_{SIA} is applied to the SIA
152 component of the velocity to increase ($E_{SIA} > 1$) the deformation induced by vertical shearing. Conversely E_{SSA} is
153 applied to the SSA component of the velocity to reduce ($E_{SSA} < 1$) the deformation due to longitudinal stresses. The
154 model parameters used in this study are the same as those used in Quiquet et al. (2021c) with the exception of E_{SIA}
155 and C_f fixed respectively to 5 (instead of 1.8) and $1.5 \cdot 10^{-6} \text{ m yr}^{-1}$ (instead of $1.5 \cdot 10^{-3} \text{ m yr}^{-1}$). Those parameters

156 have been chosen for a better match between the simulated EIS ice volume at the LGM and the geologically-
 157 constrained reconstructions (see Section 2.3).

158 The horizontal resolution used in this study is too coarse to simulate explicitly the grounding line migration
 159 (Durand et al., 2009). To circumvent this drawback, we use the analytical formulation from Tsai et al. (2015), in
 160 which the ice flux at the grounding line is computed as a function of the ice thickness and a backforce coefficient
 161 accounting for the buttressing effect of the ice shelves. In this way, a flow at the grounding line can be simulated
 162 with a lower resolution allowing time saving in the simulations. Technical details on this implementation in the
 163 GRISLI model are given in Quiquet et al. (2018).

164 At the ice shelf front, calving is computed using a simple ice thickness criterion by prescribing a minimal ice
 165 thickness set to 250 m below which ice is calved.

166 In the GRISLI model, the isostatic response to ice load is handled by an Elastic-Lithosphere-Relaxed-
 167 Asthenosphere (ELRA) model (Le Meur and Huybrechts, 1996). The relaxation time of the lithosphere is set to
 168 3000 years.

169 2.2 Climate forcing

170 We forced GRISLI with the absolute climatic fields from general circulation model (GCM) outputs of the
 171 PMIP3/PMIP4 database (Kageyama et al., 2021). All the GCMs for which LGM simulations were available at the
 172 time of writing the manuscript have been selected (see Table 1).

173 **Table 1:** PMIP3 and PMIP4 models used to force GRISLI. The fourth column indicates the choice of the ice sheet
 174 boundary condition at the LGM for each GCM simulation. ice sheet reconstructions used as a boundary condition
 175 of the GCM simulations at the LGM.

model	References	PMIP/CMIP	Boundary condition
MPI-ESM-P	Adloff et al. (2018)	CMIP5 PMIP3	PMIP3 ice sheet
MRI-CGM3	Yukimoto S et al. (2012)	CMIP5 PMIP3	PMIP3 ice sheet
MIROC-ESM	Sueyoshi et al. (2013)	CMIP5 PMIP3	PMIP3 ice sheet
CNRM-CM5	Voldoire et al. (2013)	CMIP5 PMIP3	PMIP3 ice sheet
GISS-E2-R	Ullman et al. (2014)	CMIP5 PMIP3	PMIP3 ice sheet
FGOALS-g2	Zheng and Yu (2014)	CMIP5 PMIP3	PMIP3 ice sheet
IPSL-CM5A-LR	Dufresne et al. (2013)	CMIP5 PMIP3	PMIP3 ice sheet
IPSL-CM5A2	Sepulchre et al. (2020)	CMIP6 PMIP4	ICE-6G_C
MIROC-ES2L	Hajima et al. (2020)	CMIP6 PMIP4	ICE-6G_C
MPI-ESM1.2	Mauritsen et al. (2019)	CMIP6 PMIP4	ICE-6G_C

176

177

178 Monthly surface air temperatures and solid monthly precipitation are used to compute the surface mass balance
 179 defined as the difference between snow/ice accumulation and ablation. Ablation is calculated using a positive
 180 degree-day (PDD) method following the formulation of Tarasov and Peltier (2002), where the degree-day factors,

181 C_{ice} and C_{snow} , depend on the mean July surface air temperature. Snow accumulation is calculated from the total
 182 precipitation (rain and snow), considering only months where monthly temperatures are under the melting point.

183 Due to the differences between GCM and GRISLI resolutions, the GCM outputs are bi-linearly interpolated onto
 184 the ice sheet model grid. In addition, to account for orography differences between GRISLI and the GCMs, the
 185 surface air temperatures of the GCMs are corrected using a constant vertical temperature gradient $\lambda = 7 \text{ }^\circ\text{C km}^{-1}$:

$$186 \quad T(t)_{GRISLI} = T_{GCM}^{LGM} - \lambda(S(t) - S_{GCM}^{LGM}) \quad (4)$$

187 where $T(t)_{GRISLI}$ is the time-dependent surface air temperature at the surface elevation $S(t)$ simulated by the ice
 188 sheet model, and T_{GCM}^{LGM} and S_{GCM}^{LGM} are the LGM surface air temperature and orography computed by the GCMs.
 189 This temperature correction induces a change in precipitation which is computed following the Clausius-Clapeyron
 190 formulation for an ideal gas:

$$191 \quad pr(t)_{GRISLI} = pr_{GCM}^{LGM} * \exp(\omega * (T(t)_{GRISLI} - T_{GCM}^{LGM})) \quad (5)$$

192 where $pr(t)_{GRISLI}$ is the precipitation calculated by GRISLI at each time step and pr_{GCM}^{LGM} is the LGM precipitation
 193 computed by the GCM and interpolated on the GRISLI grid. ω is the precipitation ratio to temperature change and
 194 is fixed to $0.11 \text{ }^\circ\text{C}^{-1}$ (Quiquet et al., 2013).

195 Following DeConto and Pollard (2012), the sub-shelf melt rate (OM) is computed using ocean temperature and
 196 salinity:

$$197 \quad OM = K_t \frac{\rho_w C_w}{\rho_i L_f} |T_o - T_f| (T_o - T_f) \quad (6)$$

198 where K_t is called the transfer factor and is set to $7 \text{ m yr}^{-1} \text{ }^\circ\text{C}^{-1}$ in the baseline experiments as in DeConto and
 199 Pollard (2012), ρ_w the ocean water density, ρ_i ice density, L_f the latent heat of ice fusion, C_w the specific heat of
 200 ocean water and T_o is the local ocean temperature. T_f is the local freezing point temperature, depending on the
 201 ocean salinity (S) and computed by the Beckmann and Goosse (2003) parameterization:

$$202 \quad T_f = 0.0939^\circ\text{C} - S \times 0.057^\circ\text{C} + z \times 7.6410^{-4}^\circ\text{C} \quad (7)$$

203 where z is the ocean depth.

204 A difficulty related to the oceanic forcing fields is that the GCMs do not provide any oceanic information outside
 205 their land-sea mask and under the ice shelves. To fill these gaps, we performed a classical near neighbour horizontal
 206 extrapolation of temperature and salinity except that we perform this extrapolation within 10 sectors
 207 independently. These sectors roughly correspond to drainage basins (Fig. S1). The definition of these basins is
 208 based on bedrock topographic features and LGM ice elevation and is somehow comparable to the approach
 209 followed by Zwally et al. (2015) for Antarctica. The horizontal extrapolation is performed for each individual
 210 vertical layer, without any vertical interpolation. This extrapolation method provides information on temperature
 211 and salinity within the entire ice shelf cavity for each vertical level of the GCMs. These temperature and salinity
 212 fields are then used to compute the sub-shelf melt rate (Eq. 6), using a linear vertical interpolation between the two
 213 oceanic layers bounding the ice shelf depth. The only exception is when the PMIP3/PMIP4 simulations do not

214 provide data in a given sector. In this case, a constant and homogeneous basal melting value of 0.1 m yr^{-1} is
 215 prescribed. This mainly occurs in the continental southern flanks of the Eurasian ice sheet.

216 In GRISLI, each grid point can either be a floating or a grounded ice point. To account for the fact that the sub-
 217 shelf melt rate is higher in the vicinity of the grounded line (Beckmann and Goose, 2003) and due to the coarse
 218 resolution of the model, we apply a fraction of the neighboring floating sub-shelf melt rate to the last grounded
 219 point as in De Conto and Pollard (2012). This approach allows to take the potential influence of the ocean into
 220 account.

221 The main parameters and parameterizations used in this study are shown in Table 2 and Table 3.

222 Table 2: Model parameters of the GRISLI ice-sheet model used in this study

Parameters	Identifier name	Value
Enhancement factor (SIA)	E_{SIA}	5
Enhancement factor (SSA)	E_{SSA}	1
Atmospheric temperature lapse rate	λ	$7 \text{ }^\circ\text{C km}^{-1}$
Precipitation ratio to temperature change	ω	$0.11 \text{ }^\circ\text{C}^{-1}$
Oceanic heat transfer factor	K_t	$7 \text{ m yr}^{-1} \text{ }^\circ\text{C}^{-1}$
Thickness threshold for the calving criterion	H_{cut}	250 m
Relaxation time of the asthenosphere	R_{time}	3000 years
Basal drag parameter	C_f	$1.5 \cdot 10^{-6} \text{ m yr}^{-1}$

223

224 Table 3: Parameterizations of the GRISLI ice-sheet model used in this study

Parameterizations	References
Positive degree-days	Tarasov and Peltier (2002)
Basal melting below ice shelves	Deconto and Pollard (2012)
Flux at the grounding line	Tsai et al. (2015)
Basal friction law	Linear law / Weertman (1957)

225

226 2.3 LGM equilibrium

227 As mentioned above, the main objective of the present paper is to investigate the mechanisms responsible for the
 228 EIS retreat from its LGM configuration. To do this, a preliminary step is to build the EIS at the LGM.

229 We performed ten 100 000-year spin-up experiments (one for each GCM) forced by a constant LGM climate
 230 provided by the ten GCMs. Simulations start with no ice sheet and the eustatic sea level is prescribed at 120 m
 231 below the present level. The initial bedrock topography corresponds to the present-day topography from ETOPO1
 232 (Amante et al., 2009). This procedure is required to obtain internal ice sheet conditions in equilibrium with the
 233 climate forcing and to examine whether the LGM climate can build and maintain the EIS when it is used as input
 234 to the GRISLI ice sheet model. From this climate forcing ensemble, we only selected those leading to LGM ice
 235 sheets in a reasonable agreement with the most credible ice extent in the DATED-1 database (Hughes et al., 2016)

236 and with the geologically-constrained ice thickness reconstructions, namely ICE-6G_C (Peltier et al., 2015),
237 GLAC-1D (Briggs et al., 2014; Tarasov et al., 2012; Tarasov and Peltier, 2002), and ANU (Lambeck et al., 1995,
238 1996, 2010).

239 2.4 Sensitivity experiments

240 To quantify the relative importance of the three main drivers (i.e., surface mass balance, sub-shelf melt rate, and
241 sea level) of the EIS retreat, we applied time-constant perturbations on the atmospheric and oceanic GCM forcings,
242 and we changed the prescribed sea level. The perturbed simulations are run for 10000 years. We analysed the
243 response at year 1000 of the simulation to investigate the impacts of climate changes that may have occurred at
244 the beginning of the deglaciation and at year 10,000 to examine the sensitivity of EIS on longer time scales.

245 In the first series of experiments (EXP1), we investigate the effect of SMB changes by increasing surface air
246 temperatures. During the last deglaciation (21 – 8 ka), the mean annual global surface air temperature increased
247 by $4.5^{\circ} \pm 0.9^{\circ}$ (Annan et al., 2022). In order to simulate a range of anomalies representative of the onset of the last
248 deglaciation, we chose to apply perturbations from 1 to 5 °C to the mean annual GCM forcing fields, without
249 accounting for related changes in precipitation (see Eq 5). The increase in precipitation in response to increased
250 temperatures (Eq. 5) is considered in the second set of experiments (EXP2).

251 The third series of experiments (EXP3) is designed to assess the role of oceanic forcing on the EIS stability.
252 Because the basal melting below the ice shelves depends linearly on the Kt transfer coefficient and is a quadratic
253 function of the oceanic temperatures, we performed two sub-series of experiments by modifying either the Kt
254 values (EXP3.1) without modifying the oceanic temperatures, or by applying perturbations to the oceanic
255 temperatures (EXP3.2). Observations below the Antarctic ice shelves show that the basal melting rate ranges from
256 0 to 35 m yr⁻¹ for oceanic temperatures between -2 °C and 2 °C (Holland et al., 2008). This wide range of basal
257 melting rate values reflects the complexity of such a process that can only be partially represented with simple
258 parameterizations (Eq. 6). The Kt coefficient is thus largely uncertain. Therefore, to investigate changes in the EIS
259 sensitivity to the amplitude of basal melting, we first use a wide range of values for this transfer coefficient, i.e.
260 between 10 and 50 m yr⁻¹°C⁻¹.

261 The mean global sea surface temperature anomaly inferred from the MARGO project (MARGO project members,
262 2009) between the Late Holocene and the LGM is $1.9 \pm 1.8^{\circ}\text{C}$ consistent with the findings ($\sim 2.7^{\circ}\text{C}$) of Tierney et
263 al. (2020). In the early phase of the deglaciation, the ocean warming was probably less than that of the Late
264 Holocene. Therefore, for the EXP3.2 experiments, we first apply perturbations of 0.5°C, 1.0°C, 1.5°C to the
265 oceanic temperatures (same perturbation on all vertical levels) and we fix the Kt coefficient to 7 m °C⁻¹ yr⁻¹. In the
266 transient simulation of the last deglaciation performed by Liu et al. (2009), large increases in oceanic temperatures
267 are obtained. For example, a +9°C warming is obtained in the BJR sector at 500-600 m ocean depth and almost
268 7.5°C in the SA sector at 400-500 m. To reproduce the large increase in the subsurface ocean temperature obtained
269 in Liu et al. (2009), we performed additional sensitivity experiments with perturbations of 7.5°C and 10°C applied
270 in the entire oceanic column.

271 Atmospheric and oceanic temperatures are the two main factors potentially responsible for the destabilization of
272 marine ice sheets. Thus, the fourth series of experiments (EXP4) combines surface air temperature perturbations
273 ($\Delta T = +2^{\circ}\text{C}$, $+3^{\circ}\text{C}$, and $+4^{\circ}\text{C}$) with basal melting rate perturbations ($Kt = 10, 15$ and $25 \text{ m yr}^{-1} \text{ }^{\circ}\text{C}^{-1}$).

274 In the fifth set of experiments (EXP5), we also explore the EIS sensitivity to sea level. Indeed, sea level rise favors
275 the retreat of the grounding line and is therefore another potential driver of the MISI. At the beginning of the
276 deglaciation, the global sea level increased by more than 10 m (Carlson and Clark, 2012) raising the global sea
277 level from -120 m to -110 m compared to the present-day eustatic sea level. This abrupt change may have played
278 an important role in the destabilisation of the ice sheet. On the other hand, Gowan et al., (2021) shows that the
279 local sea level around the EIS margin displays a significant spread at the LGM, from -70 m to -140 m, compared
280 to the present-day level and can abruptly change in response to variations in the land-ice mass distribution.
281 Consequently, to better explore the EIS sensitivity to both global mean sea level and local sea level at the beginning
282 of the last deglaciation, we apply moderate (-115 m, -110 m, and -105 m) and large (-90 m, -60 m, -30 m, and 0 m)
283 sea level perturbations with respect to the present day.

284 **3. Available ice sheet reconstructions and ice streams signature**

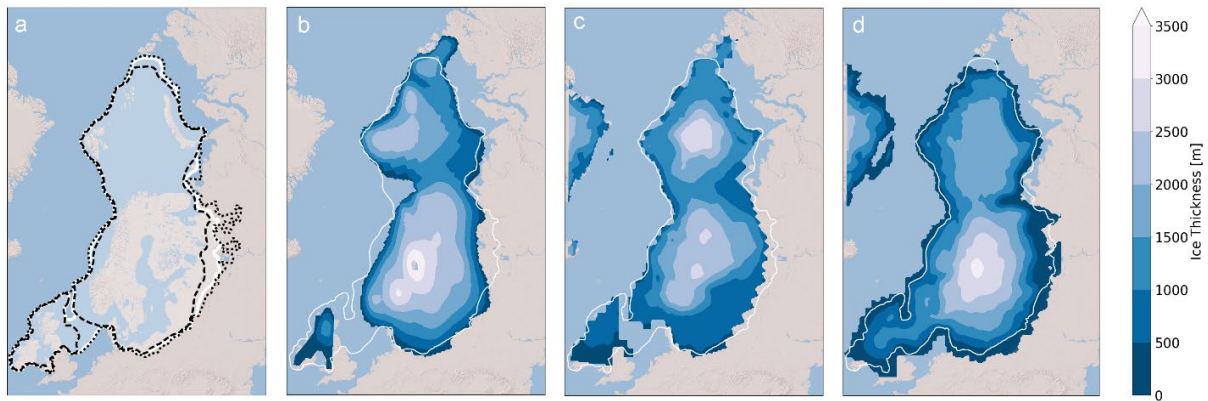
285 **3.1 Ice sheet geometry**

286 The DATED-1 database is based on evidence found in the existing literature and retrieved from various geological
287 materials (e.g., terrestrial plant macrofossils, foraminifera, speleothems, bones...) analysed with a range of dating
288 methods. Based on these data, the DATED-1 compilation provides three different scenarios for the maximal,
289 minimal and most credible EIS extent. The GLAC-1D, ICE-6G_C, and ANU reconstructions are based on inverse
290 modeling approaches constrained by GPS data, relative sea level and geomorphological data.

291 The main differences in the three DATED-1 scenarios at the LGM (Hughes et al., 2016) are related to the potential
292 BIIS-FIS connection (or disconnection), the southern continental limit of the FIS and the eastern limit of BKIS
293 (Fig. 2a). Only the minimum scenario suggests the absence of ice between the BIIS and FIS.

294 The GLAC-1D reconstruction agrees well with the most credible DATED-1 scenario, despite a slightly greater ice
295 extent in most of the Fennoscandian regions and a smaller extent in the Taymyr Peninsula (in the easternmost part
296 of the BKIS, Fig. 2d). This contrasts with the ANU and ICE-6G_C reconstructions whose ice limit goes beyond
297 that of the most credible DATED-1 scenario.

298 The differences between the three geologically-constrained reconstructions are due to differences in the inverse
299 methods used to estimate the ice thickness, to the geological and geomorphological data considered to infer the
300 ice extent, and to different choices regarding the Earth rheology. This translates into differences in the altitude of
301 the EIS. For example, in the ANU and GLAC-1D reconstructions, the FIS peaks at 3000-3500 m, while BKIS
302 does not exceed 2500 m (2000 m for GLAC-1D). By contrast, ICE-6G_C provides a larger ice thickness over the
303 BKIS sector (2500-3000 m) than over Fennoscandia.



304

305 **Figure 2:** a/ Ice sheet extent at the LGM derived from the DATED-1 compilation (Hughes et al., 2016). The
 306 maximum and the minimum scenarios of the ice extent are represented by the dotted and the dashed lines
 307 respectively. b/ Ice thickness at the LGM provided by the ANU reconstruction (Lambeck et al., 1995, 1996, 2010;
 308 Abe-Ouchi et al., 2015). c/ Same as b/ for the ICE-6G_C reconstruction (Peltier et al., 2015). d/ Same as b/ for the
 309 GLAC-1D reconstruction (Briggs et al., 2014; Tarasov et al., 2012; Tarasov and Peltier, 2002). In the four panels,
 310 the white line corresponds to the most credible scenario of the ice extent at the LGM derived from the DATED-1
 311 compilation (Hughes et al., 2016).

312 3.2 Ice stream signature

313 Ice streams also play a key role in ice sheet dynamics and in featuring ice sheet geometry (Pritchard et al., 2009).
 314 It is therefore crucial that the dynamics of the simulated ice sheets is consistent with reconstructions. The signature
 315 of ice streams can be inferred from geomorphological observations in the Barents Sea, in particular those of the
 316 Bjornoyrenna (BJR) and Svyataya Anna (SA) ice streams (Fig. 1) (Polyak et al., 1997; Andreassen and
 317 Winsborrow, 2009; Dowdeswell et al., 2016,2021; Szuman et al., 2021). Other geomorphological observations
 318 strongly suggest the existence of paleo ice streams in the FIS, such as the Mid-Norwegian (MN) ice stream (Stokes
 319 and Clark, 2001), and the Norwegian Channel (NC) ice stream between the FIS and BIIS (Sejrup et al., 1994;
 320 Svendsen et al., 2015; Stokes and Clark, 2001).

321 4. Results

322 4.1 LGM equilibrium

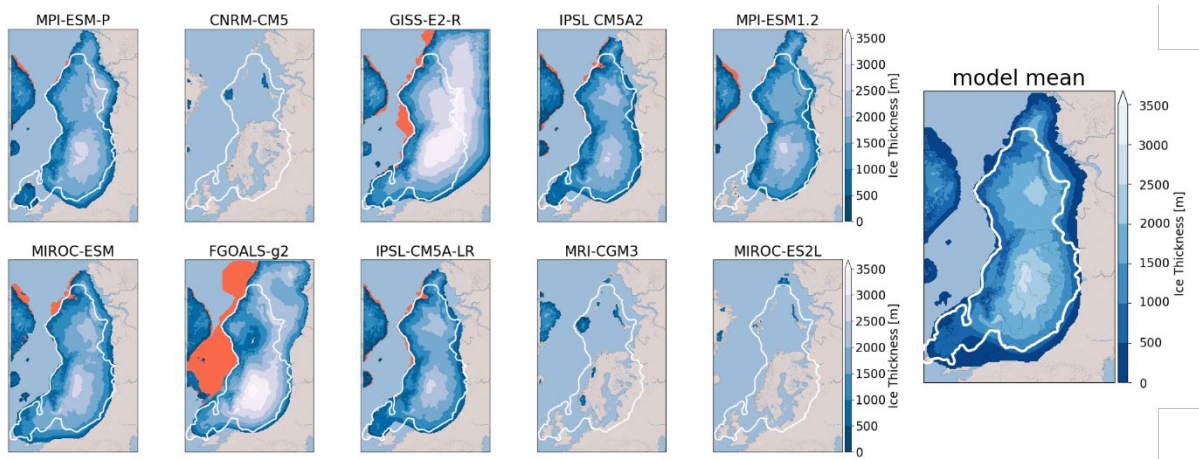
323 At the end of the 100 000-year spin-up simulations, a wide range of ice sheet geometries is obtained (Fig. 3).
 324 Simulations performed with CNRM-CM5, MRI-CGM3 and MIROC-ES2L do not succeed in building an ice sheet
 325 over Eurasia.

326 This is primarily explained by high positive summer surface air temperatures simulated by the three models in
 327 most parts of the EIS compared to the other models, with temperature anomalies ranging between +4.7°C and
 328 +11.7°C (Fig. 4). Conversely, with the GISS-E2-R and FGOALS-g2 models, significant ice thickness is built east
 329 and south of BKIS because of strong negative mean summer temperatures in this area (Fig. 4).

330 Therefore, we discarded these models and only selected those (MPI-ESM-P, MIROC-ESM, IPSL-CM5A2, IPSL-
 331 CM5-LR, and MPI-ESM1.2) providing ice sheet geometries in a relatively good agreement with the
 332 reconstructions.

333 The five selected ice sheets do not show significant differences (Fig 3). The FIS peaks at 2500-3000 m, while the
 334 BKIS is lower (2000 – 2500 m) due to a drier atmosphere compared to that overlying the Fennoscandian region
 335 (Fig. 5). The simulated FIS agrees with the ICE-6G_C reconstruction despite a flatter dome simulated with MPI-
 336 ESM-P, about 500 m lower compared to GLAC-1D and ANU. Conversely, the BKIS maximum altitude simulated
 337 by GRISLI is underestimated compared to ICE-6G_C while it is in good agreement with the two other
 338 reconstructions. The BKIS margins bordering the Greenland and Norwegian Seas and the Arctic Ocean generally
 339 match with the most credible DATED-1 scenario of the ice extent. However, in the five GRISLI simulations, the
 340 ice extent is too large in the eastern and southern edges compared to DATED-1.

341 The most likely cause of this mismatch is related to the imprint of the ice sheet reconstructions used as boundary
 342 conditions of GCM simulations. Indeed, both the ice sheet reconstruction used for PMIP3 simulations (not shown)
 343 and ICE-6G_C (Fig. 2c) used in PMIP4 runs overestimate the ice extent in the region of the Taimyr Peninsula.
 344 This results in an enhanced cooling favoring the simulated ice expansion in this area. This effect can be amplified
 345 by the projections of the ice sheet reconstructions on the coarser GCM grid that may produce an artificial spread
 346 of the ice sheet mask, causing further a too extended cooling. Another source of disagreement between DATED-
 347 1 and the simulated ice sheets can be due to the representation the jet stream and planetary waves in the coarse
 348 resolution climate models, such as the PMIP models. Indeed, such large-scale atmospheric features directly impact
 349 the simulated precipitation and temperatures and may cause too much precipitation or too much cooling if
 350 improperly represented (Löfverström and Liakka, 2018).



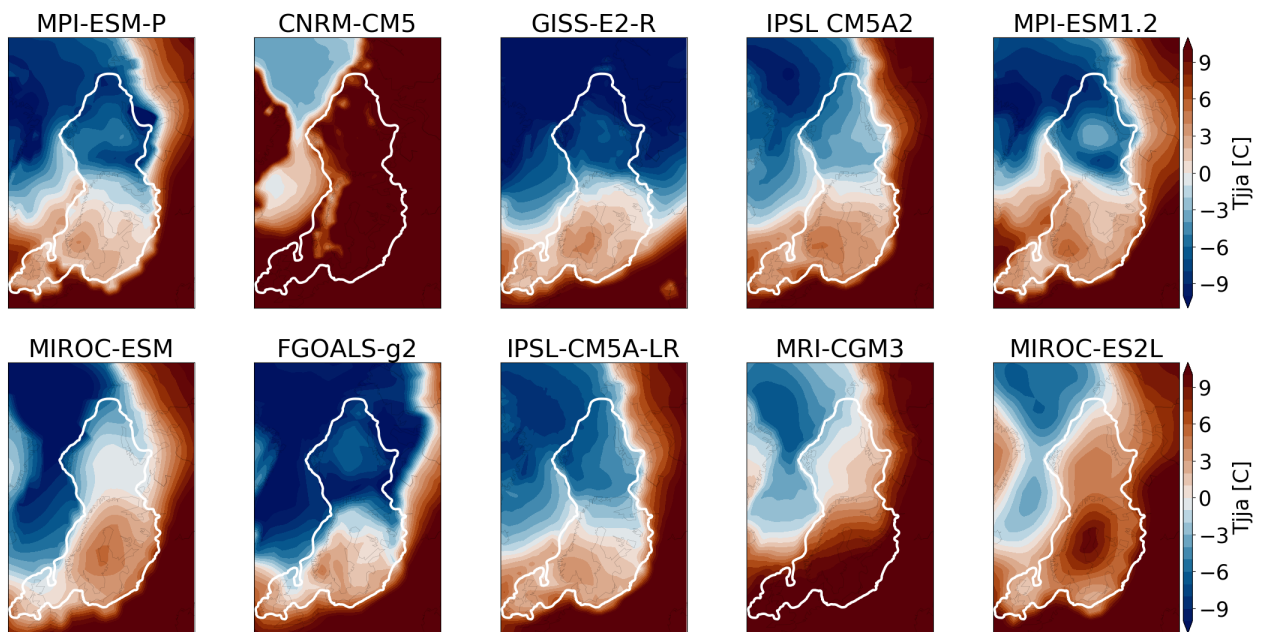
351
 352 **Figure 3:** Ice thickness at the end of the 100 000-year simulation for the different GCMs used as forcing of the
 353 GRISLI ice sheet model. The white line is the most credible extent derived from the DATED-1 compilation and
 354 the orange shaded areas are the simulated ice shelves. The multi model mean of the five selected ice sheet is shown
 355 in the right panel.

356 For the five selected GCMs, areas with high ice velocities are simulated in the BKIS region (Fig. 6). The highest
 357 velocities are obtained for the SA, BJR, NC and MN ice streams and can exceed 1000 m yr^{-1} . In addition, the BJR
 358 ice stream shows a large extension from the center of BKIS, with velocities between 75 to 200 m yr^{-1} , to the edge

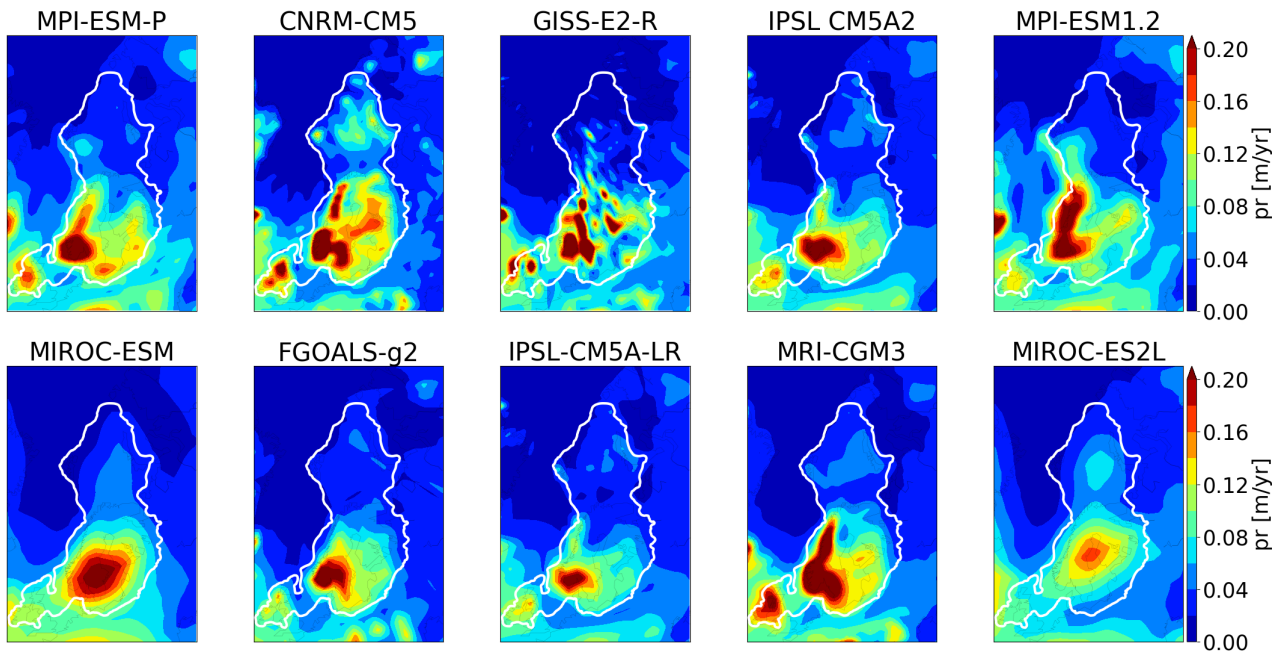
359 of BKIS. The location of the main fast flowing areas is consistent with empirical evidence based on observations
360 of submarine landforms (Dowdeswell et al., 2016; Stokes and Clark, 2001). It is also interesting to mention that
361 ice velocities of similar magnitude in the present-day Antarctic and Greenland ice sheets have been revealed thanks
362 to radar observations (Solgaard et al., 2021; Mouginot et al., 2019).

363 Overall, our five remaining simulated ice sheets show a reasonable agreement with the different reconstructions
364 constrained by geological and geomorphological observations, both in terms of ice extent and ice thickness as well
365 as dynamical characteristics. The observed differences with the reconstructions remain within the range of
366 uncertainties, which is itself illustrated by the differences between the three reconstructions GLAC-1D, ANU and
367 ICE-6G_C and by the three ice extent scenarios from the DATED-1 compilation.

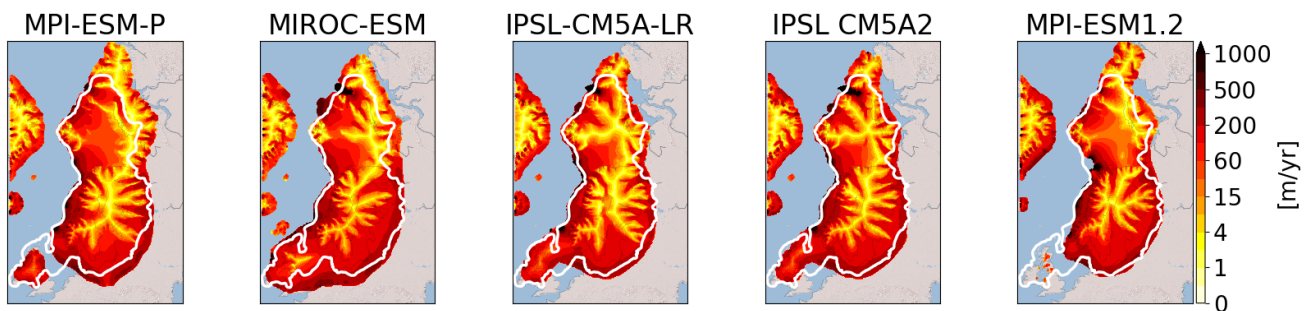
368 This allows us to use the five spin-up GRISLI experiments (forced by MPI-ESM-P, MIROC-ESM, IPSL-CM5A2,
369 IPSL-CM5-LR, and MPI-ESM1.2) as a starting point to test the sensitivity of the EIS to atmospheric, oceanic and
370 sea level forcings.



371
372 **Figure 4:** Mean summer (JJA) surface air temperature at 21 ka simulated by each GCM at the sea level and
373 interpolated on the GRISLI grid. The white line represents the ice extent as defined by the most credible DATED-
374 1 scenario.



375
376 **Figure 5:** Same as Figure 4 for the mean annual precipitation.



377
378 **Figure 6:** Simulated ice velocities at the end of the 100 000-year LGM simulation. The solid white line represents
379 the most credible ice extent from the DATED-1 compilation.

380 4.2. Sensitivity experiments

381 In the following, we investigate the sensitivity of the Eurasian ice sheet to the potential drivers of ice sheet retreat:
382 atmospheric changes responsible for SMB changes (i.e., temperature and snow accumulation to the first order),
383 oceanic changes (sub-shelf melt rate) and sea level changes.

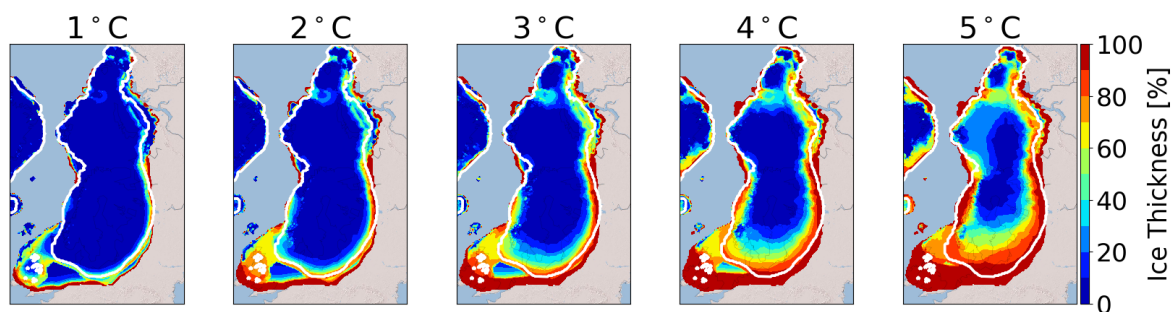
384 4.2.1 EXP1: Surface air temperature

385 The aim of this section is to investigate the sensitivity of EIS to a temperature rise. For each temperature
386 perturbation ($T_{\text{add}} = 1$ to 5°C) applied uniformly on the monthly mean surface air temperatures, Figure 7 displays
387 for the multi-model mean the percentage of the ice thickness lost after 1000 years with respect to the initial
388 configuration. The results are plotted for the largest ice sheet mask. This mask corresponds to all areas where ice
389 has been simulated in at least one of the 5 simulations. This means that multi-model means are computed with 1,
390 2, 3, 4 or 5 models involved, depending on the ice sheet mask of each individual model.

391 For $T_{\text{add}} = 1\text{ }^{\circ}\text{C}$, the response of the Eurasian ice sheets is weak, except for the British Isles sector (Fig 7) for which
 392 mean JJA temperatures of the five selected GCMs are close to the melting point (Fig. 4). Substantial ice losses are
 393 also simulated in the FIS margins for temperature rise greater than $1\text{ }^{\circ}\text{C}$ leading to a progressive retreat of the edge
 394 of the ice sheet as the temperature increases. The sensitivity of the BIIS and FIS regions to these temperature
 395 perturbations is explained by a shift from positive to negative SMB values when temperature increases (Fig. SP2).
 396 By contrast, as the BKIS is located in colder areas, larger temperature perturbations ($3\text{ to }5\text{ }^{\circ}\text{C}$) are necessary to
 397 initiate the ice sheet's retreat. The southern BKIS margin appears the most sensitive region, followed by the region
 398 of the SA ice stream. In the SA sector, ice thickness losses between 30% ($T_{\text{add}} = +3^{\circ}\text{C}$) to 50% ($T_{\text{add}} = +5^{\circ}\text{C}$)
 399 are obtained. In the BJR sector, ice losses are only simulated for large temperature perturbations.

400 However, it is worth mentioning that for a given temperature perturbation, significant differences in the behavior
 401 of the five simulated ice sheets can be observed. To illustrate these differences, we plotted for each simulation, the
 402 percentage of the ice thickness lost after 1000 years with respect to the initial configuration (Fig SP3). The most
 403 sensitive regions to surface air temperature, namely the FIS margins and the SA/BJR sectors, are the locations
 404 where inter-model differences in ice thickness losses are the most significant and are amplified with temperature
 405 increase. In the BJR sector, the retreat of the ice sheet is simulated for perturbations of 4°C with three GCM
 406 forcings (MIROC-ESM, IPSL-CM5A-LR and IPSL-CM5A2, Fig SP3), while this sector is stable with the two
 407 other forcings (MPI-ESM-P and MPI-ESM1.2) under this temperature perturbation. In the SA sector, the MIROC-
 408 ESM-P forcing produces a retreat from a temperature anomaly of 2°C , but for the IPSL-CM5A-LR and IPSL-
 409 CM5A2 forcings the retreat is only triggered for $T_{\text{add}} = 3\text{ }^{\circ}\text{C}$. By contrast, the two versions of the MPI-ESM
 410 produce a more stable ice sheet in the SA sector since, even with a $5\text{ }^{\circ}\text{C}$ temperature perturbation, the ice retreat
 411 is not triggered within the 1000 years of simulation.

412 The lower sensitivity of BJR sector, compared to the SA sector, can be explained (at least partly) by the topography
 413 differences between these two regions. Actually, the initial topography of each GCM (not shown) exhibits a trough
 414 in the SA sector which does not appear in the region of the BJR ice stream. The lower surface topography in the
 415 SA sector is accompanied by higher surface temperatures and thus to larger ice losses when temperature
 416 perturbations are applied (Fig. SP3). Moreover, the difference in the sensitivity of the BJR and SA sectors can be
 417 also explained by the higher precipitation rate in the BJR sector (between $0.2\text{ to }0.5\text{ m yr}^{-1}$ for the BJR ice stream
 418 and less than 0.2 m yr^{-1} for the SA sector, Fig. 5), which can partly counteract the effect of temperature increase
 419 on ice mass loss.



420
 421 **Figure 7:** Multi-model mean of the ice thickness lost after 1000 GRISLI model years in the EXP1 experiments
 422 with respect to the ice thickness of the LGM ice sheet (red: 100% lost). The results are plotted on the largest ice

423 sheet mask. The white line corresponds to the common ice sheet mask of the five models, i.e., where the multi-
424 model mean is computed on the 5 models.

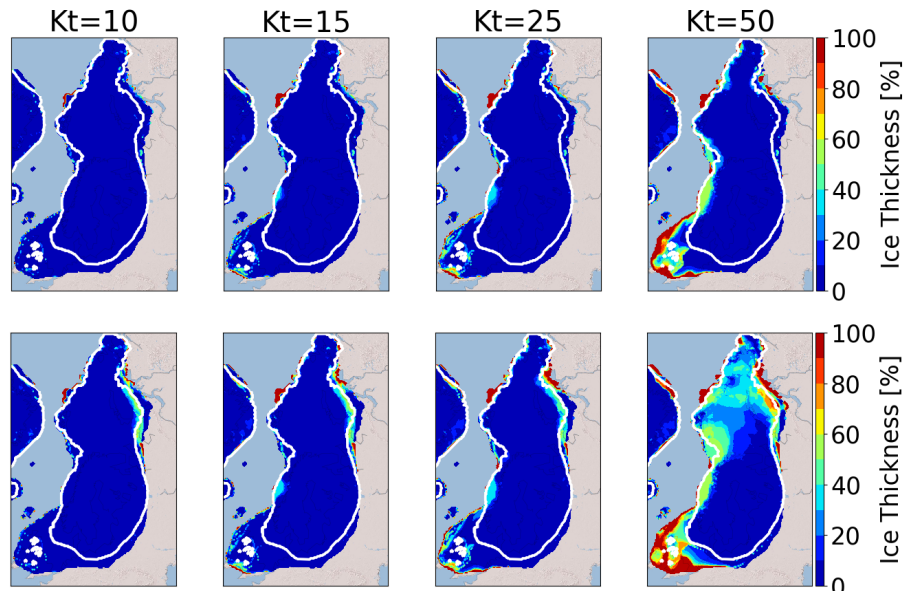
425 To better understand the effect of precipitation on the EIS stability, the EXP2 combines the precipitation and
426 surface air temperature perturbations. The results obtained in the EXP2 experiments are shown in figure SP4. For
427 BIIS and FIS, a similar behavior to EXP1 is observed, albeit with less ice melt due to increased accumulation as a
428 result of increased temperatures. On the contrary, in EXP2, a large difference with EXP1 is simulated for BKIS,
429 where only the ice sheet margins show sensitivity to increased temperature and precipitation. While an inland ice
430 loss between 20% and 50% was simulated in EXP1 in some places, it is generally limited to less than 10% in
431 EXP2. This result shows the significant role of precipitation to counteract the ice loss due to an increase in surface
432 air temperature.

433 **4.2.2 EXP3: Basal melting**

434 Besides changes in SMB, another factor that can destabilize a marine ice sheet is the basal melting under the ice
435 shelves (Pritchard et al., 2012). In the LGM experiments, the numerical Kt value is fixed to $7 \text{ m } ^\circ\text{C}^{-1} \text{ yr}^{-1}$ and leads
436 to basal melting rates in the BJR and SA sectors of 3.1 m yr^{-1} and 0.7 m yr^{-1} respectively. To investigate the effect
437 of increased basal melting that likely occurred during the last deglaciation as a response of increased ocean
438 temperatures, we performed sensitivity experiments by first changing the Kt value (EXP3.1). The sensitivity to
439 oceanic temperatures (EXP3.2) will be discussed later.

440 Figure 8 displays the percentage of ice thickness losses (with respect to the initial configuration) for Kt ranging
441 from $10 \text{ m } ^\circ\text{C}^{-1} \text{ yr}^{-1}$ to $50 \text{ m } ^\circ\text{C}^{-1} \text{ yr}^{-1}$. After 1000 years of simulation, no change in ice thickness is observed for Kt
442 = $10 \text{ m } ^\circ\text{C}^{-1} \text{ yr}^{-1}$. For higher Kt values ($15 \text{ m } ^\circ\text{C}^{-1} \text{ yr}^{-1}$ and $25 \text{ m } ^\circ\text{C}^{-1} \text{ yr}^{-1}$), ice losses between 30% to 40% are
443 simulated in the MN ice stream sector, and 100% of the ice shelf in the south of SA sector is melted (see Fig 3
444 showing the presence of ice shelves at the end of the spin-up experiment). This corresponds to basal melting rates
445 (multi-model mean) near the grounding line ranging from 7.5 m yr^{-1} (Kt = $15 \text{ m } ^\circ\text{C}^{-1} \text{ yr}^{-1}$) to 10.4 m yr^{-1} (Kt = 25
446 $\text{ m } ^\circ\text{C}^{-1} \text{ yr}^{-1}$) in the MN sector and from 1.7 m yr^{-1} (Kt = $15 \text{ m } ^\circ\text{C}^{-1} \text{ yr}^{-1}$) to 2.9 m yr^{-1} (Kt = $25 \text{ m } ^\circ\text{C}^{-1} \text{ yr}^{-1}$) in the SA
447 sector. However, these changes are restricted to small areas, and the ice loss is not significant enough to firmly
448 indicate a noticeable sensitivity to basal melting. Perturbations with Kt values above $25 \text{ m } ^\circ\text{C}^{-1} \text{ yr}^{-1}$ are necessary
449 to observe significant changes in the EIS configuration. In particular, for Kt = $50 \text{ m } ^\circ\text{C}^{-1} \text{ yr}^{-1}$, the ice is entirely
450 melted near the BIIS margins, and less than 50 % of the ice remains in the regions of MN, SA and BJR ice streams.
451 Nonetheless, only the simulations forced by MPI-ESM-P, MPI-ESM1.2 and MIROC-ESM show a sensitivity to
452 basal melting in BJR, MN and SA sectors (Fig. SP5). Depending on the GCM forcing, the simulated basal melting
453 values range between 25.7 and 28.7 m yr^{-1} , 24.4 and 28.2 m yr^{-1} and between 11.2 and 13.4 m yr^{-1} for the BJR,
454 MN and SA sectors respectively. By contrast, very small values are obtained with IPSL-CM5A2 (0.2 m yr^{-1} 0.5 m
455 yr^{-1}) and IPSL-CM5A-LR models (0.5 m yr^{-1}). This can be explained by the cold oceanic temperatures near the
456 BJR sector compared to those simulated by the three other GCMs (Fig SP6). These results show that the basal
457 melting has the ability to destabilize the BKIS when it exceeds a certain threshold. Results inferred from the
458 simulations forced by MPI-ESM-P, MPI-ESM1.2 and MIROC-ESM suggest that this threshold is obtained for Kt
459 values between 25 and $50 \text{ m } ^\circ\text{C}^{-1} \text{ yr}^{-1}$, corresponding to basal melting rates at the grounding line between 10.4 m
460 yr^{-1} and 28.7 m yr^{-1} for the BJR sector and between 6.2 and 13.4 m yr^{-1} for the SA sector. By comparison, a basal
461 melting rate of 22 m yr^{-1} has been observed thanks to radar measurements in the mouth of the Mercer/Whillans Ice

462 Stream located in the West Antarctic ice sheet (Marsh et al., 2016). Providing that K_t values are greater than 25
 463 $\text{m}^\circ\text{C}^{-1} \text{yr}^{-1}$ (or close to $50 \text{ m}^\circ\text{C}^{-1} \text{yr}^{-1}$), the region of the BJR ice stream responds to basal melting perturbations
 464 with basal melting rates similar to those observed in some parts of WAIS. However, the ice loss is restricted to the
 465 very edge of the ice sheet and the BKIS retreat is negligible. This raises the question as to whether the basal melting
 466 exerts a stronger influence on longer time scales. Therefore, we also investigated the ice sheet behavior after 10 000
 467 model years.



468

469 **Figure 8:** Multi-model mean of the ice thickness lost after 1000 (top) and 10 000 (bottom) GRISLI model years
 470 in the EXP3.1 experiments with respect to the ice thickness of the LGM ice sheet. (red: 100% lost). The white line
 471 corresponds to the common ice sheet mask of the five models, i.e., where the multi-model mean is computed on
 472 the 5 models.

473 A similar behavior is observed after 10 000 years for K_t between 10 and 25 $\text{m}^\circ\text{C}^{-1} \text{yr}^{-1}$, with the exception of the
 474 southern part of BKIS bordering the Kara Sea where a 30% to 50% ice thickness decrease, with respect to the
 475 initial one, is obtained. For $K_t=50 \text{ m}^\circ\text{C}^{-1} \text{yr}^{-1}$, more than 40% of ice loss is simulated for BKIS, and up to 60% in
 476 the BJR sector. As previously mentioned, this large ice thickness decrease in the center of BKIS is highly GCM-
 477 dependent, and is only observed in simulations forced by the MIROC and MPI models (Fig. SP5

478 As the basal melting parameterization is expressed as a quadratic function of the oceanic temperatures, we may
 479 expect a different sensitivity of EIS when the oceanic temperatures increase (EXP3.2). Results of the EXP3.2
 480 experiments are shown in figure SP7. Perturbations of oceanic temperatures between $+0.5^\circ\text{C}$ and $+1.5^\circ\text{C}$ lead to
 481 basal melting rates at the grounding line of the BJR sector of less than 3.8 m yr^{-1} . This is well below the threshold
 482 suggested by the results of the EXP3.1 experiments (between 10.4 and 30 m yr^{-1}), and no significant ice loss is
 483 simulated after 10 000 years of simulation.

484 For larger perturbations ($+7.5^\circ\text{C}$ and $+10^\circ\text{C}$), larger values of the basal melting rates are obtained in the BJR (11.6
 485 and 17.5 m yr^{-1}), in the SA (10.8 and 15.6 m yr^{-1}) and in the MN sectors (11.5 and 17.4 m yr^{-1}) after 10 000 model
 486 years. A perturbation of 7.5°C does not trigger the ice retreat because of a too low basal melting. By contrast, when
 487 the perturbation reaches $+10^\circ\text{C}$, a similar behavior to that simulated with $K_t=50 \text{ m}^\circ\text{C}^{-1} \text{yr}^{-1}$ (EXP3.1) is obtained.

488 On the other hand, for simulations forced by IPSL-CM5A2 and IPSL-CM5A-LR, an increase in oceanic
489 temperatures of +10°C allows us to observe a sensitivity of BKIS in the SA sector (see Fig SP8) after 1000 years
490 of simulations, which leads to a total retreat of the eastern part of BKIS after 10000 years.

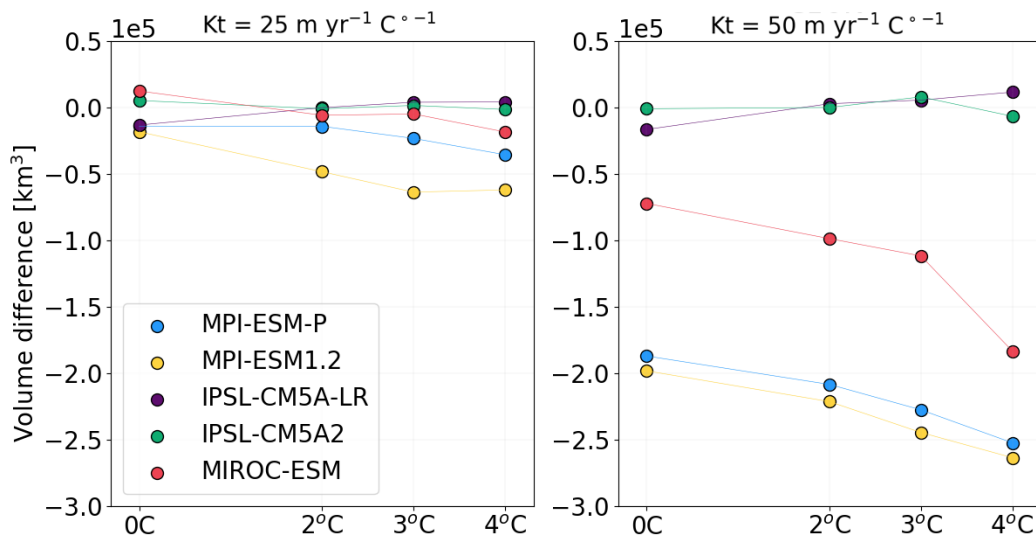
491 These results show that the BJR, MN and SA regions are sensitive to sub-shelf melting providing that the basal
492 melt exceeds a certain threshold obtained for Kt values greater than 25 m °C⁻¹ yr⁻¹ (and greater than 10 m °C⁻¹ yr⁻¹
493 for the MN sector) or for a rise in oceanic temperature greater than 7.5°C. From the combination of EXP3.1 and
494 EXP3.2 experiments, it appears that the threshold is between 11.6 m yr⁻¹ and 17.5 m yr⁻¹ for the BJR sector,
495 between 6.2 and 13.4 m yr⁻¹ for the SA sector and lower than 7.5 m yr⁻¹ for the MN sector. Moreover, our results
496 also suggest that the large retreat of one single ice stream has the ability to favor the total retreat of the whole of
497 BKIS

498 **4.2.3 EXP4: Combined effects of basal melting and surface air temperatures**

499 Results presented in the previous section suggest that sub-shelf melting has only a poor impact on the EIS
500 destabilization for Kt perturbations below a certain threshold estimated to lie between 25 and 50 m °C⁻¹ yr⁻¹, or
501 below a +10°C increase of oceanic temperatures. However, increases in surface melting due to atmospheric
502 warming may lead to changes in the geometry of the grounded ice sheet and floating ice shelves. In turn, changes
503 in the EIS configuration may alter the EIS sensitivity to basal melting. To test this hypothesis, we combined surface
504 air temperature perturbations with basal melting perturbations (EXP4) and compared the results with those of the
505 EXP1 experiments. Figure 9 displays the difference in the total BKIS ice volume after 1000 years between EXP4
506 and EXP1 experiments (ΔV_{4-1}) for different surface atmospheric temperature perturbations ($\Delta T = +2^\circ\text{C}$, $+3^\circ\text{C}$ and
507 $+4^\circ\text{C}$) and Kt values fixed to 25 and 50 m °C⁻¹ yr⁻¹ (negatives values are associated to a greater ice loss in EXP4
508 than in EXP1). For both Kt perturbations (Kt = 25 and 50 m °C⁻¹ yr⁻¹), no significant difference in the ΔV_{4-1} values
509 (computed for the different ΔT perturbations) is observed in simulations forced by IPSL-CM5A2 and IPSL-
510 CM5A-LR. This illustrates the poor sensitivity of BKIS to basal melting with the IPSL climate forcings. As
511 explained in section 4.2.2, this low sensitivity is due to the cold oceanic temperatures simulated in both IPSL
512 models (see Fig. SP6). For the three other simulations (forced by MIROC-ESM, MPI-ESM-P, and MPI-ESM1.2),
513 the ice volume difference is clearly amplified with higher ΔT levels, especially when the Kt transfer coefficient is
514 higher. For example, for Kt=50 m °C⁻¹ yr⁻¹, the difference in ΔV_{4-1} values between the initial ice sheet configuration
515 ($\Delta T = 0^\circ\text{C}$) and $\Delta T = 4^\circ\text{C}$ is ~60 000 km³ with MPI-ESM-P, against ~20 000 km³ when Kt=50 m °C⁻¹ yr⁻¹. A
516 similar behavior is observed for simulations forced by MIROC-ESM (~110 000 km³) and MPI-ESM1.2 (~60 000
517 km³). To better illustrate the impact of the combination of both temperature and basal melting perturbations, we
518 plotted the evolution of ice loss every 1kyr as simulated in the EXP1 ($\Delta T = +4^\circ\text{C}$), EXP3 (Kt=50 m °C⁻¹ yr⁻¹) and
519 EXP4 experiments in figures SP9 to SP11. For the simulation forced by MIROC-ESM (Fig. SP11), the largest part
520 of the deglaciation signal is dominated by increased atmospheric temperatures in the EXP4 (see Fig SP11).
521 Simulations forced by MPI-ESM-P and MPI-ESM1.2 have a different behaviour (Figs SP9 and SP10) and show a
522 significant difference between EXP1 and EXP4 and between EXP3 and EXP4. In the EXP3 experiment, the SA
523 sector appears to be highly sensitive, mainly due to high ocean temperatures ($> 3^\circ\text{C}$, see fig SP6) in contrast to the
524 BJR sector where only a part has deglaciated after 10 000 years. However, in the EXP4 experiment, in which near-
525 surface temperature and basal melting are combined, BKIS starts to retreat after 1000 years and has almost entirely

526 melted after 10 000 years. This suggests that the BKIS deglaciation is initially triggered by surface warming but
 527 is further amplified by basal melting.

528



529

530 **Figure 9:** Differences of the ice volume lost between EXP4 and EXP1 (ΔV_{4+1}) after 1000 years for $Kt=25 \text{ m } ^\circ\text{C}^{-1}$
 531 yr^{-1} (left) and $Kt=50 \text{ m } ^\circ\text{C}^{-1} \text{ yr}^{-1}$ (right).

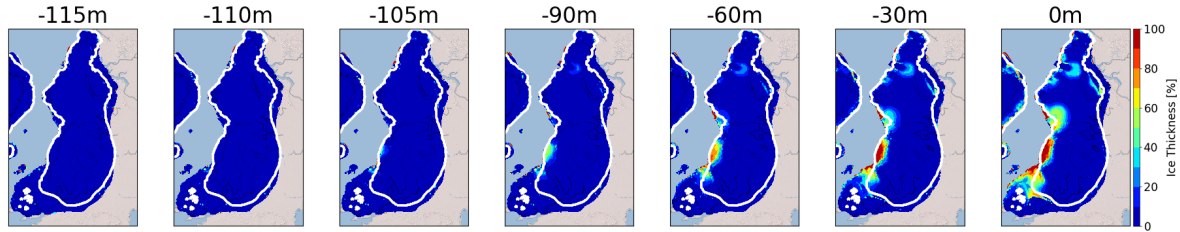
532 **4.2.5 Exp5: Sea level**

533 In the previous simulations, the sea level forcing was fixed to -120 m (with respect to the present-day eustatic sea
 534 level), corresponding to the estimated eustatic level at the LGM (Peltier et al., 2002). In this series of experiments,
 535 we quantify the sensitivity of the EIS to different sea level forcings.

536 The multi-model mean difference between the ice thickness after 1000 GRISLI model years and the initial ice
 537 thickness (sea level = -120 m) is displayed in Figure 10 for the different sea level elevations ranging from -115 m
 538 to 0 m. After 1000 years of simulation, for sea levels ranging from -115 m to -105 m, no significant differences
 539 are observed with respect to the reference simulation (i.e., -120 m). For larger perturbations, the MNIS sector
 540 appears to be the most sensitive. As an example, for a sea level of -90 m, an ice loss of ~40 % is simulated in this
 541 area, and an almost complete retreat is obtained for a sea level higher than -60m, with an ice thickness decrease of
 542 up to 80%-100%. Although sea level elevations of -90 m and -60 m are considerably larger than the global mean
 543 sea level at the LGM, they are consistent with the local sea level variations that could be as high as -70 m as
 544 suggested by Gowan et al. (2021). However, for the other sectors (BJR, SA, NCIS), ice thickness decrease is only
 545 obtained for sea levels higher than -30 m which is largely out of the range advanced by Gowan et al. (2021). As a
 546 result, this series of experiments conducted with the GRISLI model suggests that the elevation of sea level has
 547 only played a marginal role at the beginning of the EIS deglaciation.

548 However, it should be noted that sea level rise can lead to changes in the geometry of the ice sheet and floating ice
 549 shelves. Therefore, these changes in the EIS configuration may influence its sensitivity to oceanic temperature
 550 perturbations. We tested this hypothesis by raising the sea level from -120 m to -110 m compared to the current
 551 level and by raising concomitantly the oceanic temperatures (+1.5°C and +10°C). Adding a sea level perturbation

552 to the oceanic temperature perturbation does not drastically change the response of the ice sheet. Differences of 6
 553 to 7 % in ice volume losses were only observed for the highest temperature perturbation (+10°C) after 10 000
 554 years for only two GCM forcings (MIROC-ESM and IPSL-CM5A2), while the differences are negligible (lower
 555 than 2%) for smaller perturbations, shorter timescales and other GCM forcings (not shown).



556
 557 **Figure 10:** Multi-model mean of the ice thickness lost after 1000 model years in the EXP5 with respect to the ice
 558 thickness of the LGM ice sheet. (red: 100% lost). The white line corresponds to the common ice sheet mask of the
 559 five models, i.e., where the multi-model mean is computed on the 5 models.

560 4.3 Sensitivity to the spin up method

561 The construction of spin-up is one of the most important factors impacting the sensitivity of the EIS. The LGM
 562 ice sheets presented in Section 4.1 were constructed under a constant LGM climate during 100 000 years. The
 563 specificity of this method is to construct ice sheets in good equilibrium with their environment. However, as
 564 outlined by Batchelor et al. (2019), the EIS was far from being in equilibrium with the climate at the LGM.

565 In order to look into the biases associated with the choice of the spin-up method, we compared the results obtained
 566 with a transient spin-up procedure. For this purpose, we reconstructed a climatology evolving from the Last
 567 Interglacial (-127 000 years) to the LGM (-21 000 years) using a multi-proxy climatic index (Quiquet et al., 2021c).
 568 In the same way as above, we used the 10 PMIP3/PMIP4 forcings shown in Table 1. As the last interglacial
 569 simulations were not available for some of the PMIP3/PMIP4 models, we made the approximation that the -127
 570 000 climate was represented by the pre-industrial climate (i.e. piControl experiments, Eyring et al., 2016).

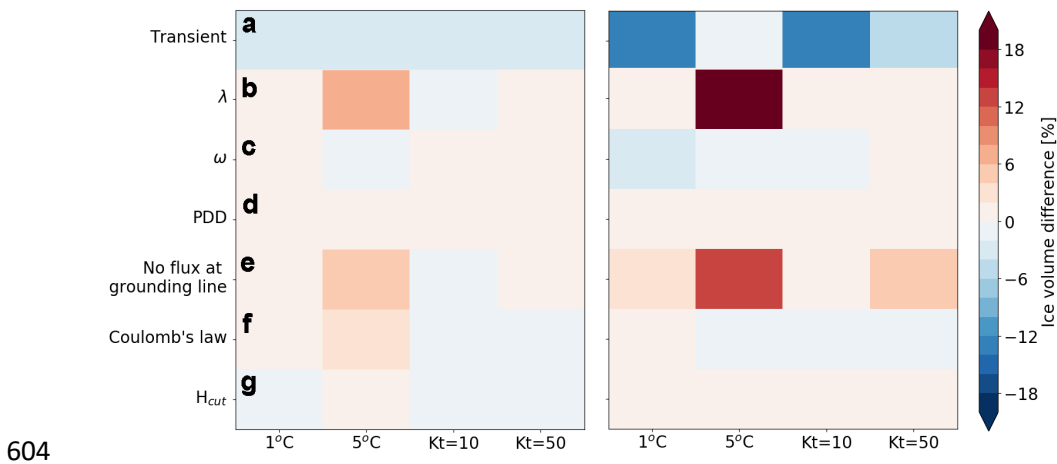
571 At the end of the of these new spin-up simulations, only 4 PMIP forcings (MPI-ESM-P, MPI-ESM1.2, IPSL-
 572 CM5A2 and IPSL-CM5A-LR) succeeding in constructing the EIS in agreement with the reconstructions (see
 573 figure SP12h). Compared to previous LGM ice sheets presented in Section 4.1, the ice extent is smaller (Fig.
 574 SP12h) and the dome of FIS is flatter with sharper edges. Furthermore, contrary to the previous method of spin-
 575 up construction (i.e. constant LGM forcing), the simulation forced by MIROC-ESM failed to form an ice sheet
 576 over the Barents Sea.

577 To assess the effect of the LGM EIS obtained after each of the transient spin-up experiment obtained with MPI-
 578 ESM-P, MPI-ESM1.2, IPSL-CM5A2 and IPSL-CM5A-LR, we applied atmospheric temperature perturbations
 579 (+1°C and +5°C, as in EXP1) and basal melting perturbations (Kt values of 10 m°C⁻¹yr⁻¹ and 50 m°C⁻¹yr⁻¹, as in
 580 EXP3.1). Finally, we compare the percentage of remaining ice volume with the reference one (i.e simulated in
 581 EXP1 and EXP3.1) and the new perturbed simulations after 1000 and 10 000 years using the following formula:

$$582 \quad \delta = \frac{V_{pert}(t=end) - V_{pert}(t=0)}{V_{pert}(t=0)} - \frac{V_{ref}(t=end) - V_{ref}(t=0)}{V_{ref}(t=0)} \quad (8)$$

583 Each term in the right-hand side of Equation (8) represents the percentage of ice volume loss in a given simulation.
 584 δ represents the difference (in %) of ice volume loss between the new simulation and the reference simulation,
 585 with V_{pert} being the ice volume for the new perturbed simulation (transient spin-up) and V_{ref} the ice volume of
 586 the EXP1 and EXP3 simulations. A negative value of V_{ice} indicates a greater retreat of EIS of the new EIS
 587 configurations (i.e. obtained with the transient spin-up method).

588 Figure 11a shows the results of the computed δ value (see Eq. 8) after 1000 (left) and 10 000 model years (right)
 589 averaged over all models for atmospheric (1°C and 5°C) and oceanic ($Kt = 10$ and $50 \text{ m}^\circ\text{C}^{-1}\text{yr}^{-1}$) perturbations.
 590 After 1000 years, no significant difference is observed between both simulations. Conversely, after 10 000 years,
 591 a difference of the order of -10% for perturbations of 1°C and $10 \text{ m}^\circ\text{C}^{-1}\text{yr}^{-1}$ is observed. This can be explained by
 592 internal processes that are not in equilibrium with the LGM climate at the end of the transient spin-up simulation.
 593 More specifically, large differences in the simulated effective pressure are obtained at the end of both spin-up
 594 experiments. In the reference spin-up simulation (constant LGM climate), there is a relatively low effective
 595 pressure since sub-glacial water has accumulated over the 100 000 year of simulation (Fig. SP13). By contrast, in
 596 the spin-up constructed by the transient method, large parts of the ice sheet are englacial for much shorter time
 597 periods with smaller amount of sub-glacial water resulting in higher effective pressure. This leads to drastically
 598 different sliding velocities among the two spin-up methods, with much smaller ice sheet velocities after the
 599 transient spin-up. During the perturbation experiments, the sub-glacial water tends to accumulate when using the
 600 transient spin-up ice sheet state. The temporal evolution in this case reflects the decrease in the effective pressure
 601 (and related increase in velocity) on top of the applied atmospheric or oceanic perturbation. The sensitivity over
 602 time scales greater than one thousand years in these new experiments is thus not directly comparable to the
 603 reference sensitivity experiments in which the effective pressure is fully equilibrated.



605 Figure 11: Multi model mean of the differences in ice volume loss between the new perturbed simulations and the
 606 reference simulations (EXP1 and EXP3) after 1000 years (left) and after 10000 years (right). Note that the multi
 607 model mean is done without the contribution of MIROC-ESM forcing for the panel a. The volume difference is
 608 calculated thanks to the equation 8.

609 4.4 Sensitivity to different GRISLI configurations

610 The results presented in Section 4.2 suggest that the EIS was primarily sensitive to atmospheric forcing at the
 611 beginning of the last deglaciation. However, we cannot exclude that this finding is specific to the choices of model

612 parameters (Table 2) and physical parameterizations (Table 3). In order to assess the extent to which the observed
 613 EIS sensitivity is driven by these choices, we conducted additional experiments with alternative values of climate-
 614 related parameters (vertical temperature gradient, the precipitation ratio to temperature change, degree-day factors
 615 in the PDD formulation). We also changed the basal friction law and removed the parameterization of the ice flux
 616 at the grounding line (Table 4). We first performed 100 000-year simulations using the same procedure as for the
 617 reference simulations (Fig. SP12a-g). Note that the CNRM-CM5, GISS-E2-R, MIROC-ES2L, FGOALS-G2 and
 618 MRI-CGM3 fail to reproduce an ice sheet in agreement with the reconstructions similarly to as our reference
 619 experiments (see Sections 4.1 and 4.2).

620 Next, we applied atmospheric temperature perturbations (+1°C and +5°C) and basal melting perturbations ($Kt =$
 621 $10 \text{ m}^\circ\text{C}^{-1}\text{yr}^{-1}$ and $50 \text{ m}^\circ\text{C}^{-1}\text{yr}^{-1}$) to evaluate the relative importance of both atmospheric and oceanic forcings with
 622 the modified GRISLI configurations.

623 **Table 4:** List of sensitivity experiments (columns 5-10) performed with changes in the standard GRISLI
 624 configuration. New values of model parameters are given in column 4 with reference values indicated in
 625 parentheses. Changes in physical parametrizations are indicated in column 2.

exp n°	GRISLI configuration changes			Spin-up methods		Perturbations experiments			
	Variables	Name	Value	Constant LGM	Transient	1°C	5°C	Kt=10	Kt=50
1	Spin-up method	-	Transient		✓	✓	✓	✓	✓
2	Vertical temp gradient	λ	$4 \text{ }^\circ\text{C km}^{-1}$ (7)	✓		✓	✓	✓	✓
3	Precip/temperature change	ω	$0.05 \text{ }^\circ\text{C}^{-1}$ (0.11)	✓		✓	✓	✓	✓
4	PDD coefficients	$C_{\text{ice,snow}}$	- 25%	✓			✓	✓	✓
5	PDD coefficients	$C_{\text{ice,snow}}$	+ 25%	✓		✓			
6	Flux at the grounding line	-	None	✓		✓	✓	✓	✓
7	Basal friction law	-	Plastic drag	✓		✓	✓	✓	✓
8	calving criterion	H_{cut}	50 m (250)	✓		✓	✓	✓	✓

626

627 4.4.1 Sensitivity to climate parameters

628 At first, we examined the sensitivity of EIS to a vertical temperature gradient of $4 \text{ }^\circ\text{C km}^{-1}$ (instead of $7 \text{ }^\circ\text{C km}^{-1}$)
 629 which is considered by Marshall et al. (2007) as the most likely value of the near-surface temperature lapse rate.
 630 Therefore, a decrease in ice thickness of 100 meters results in a decrease in atmospheric temperature of $0.4 \text{ }^\circ\text{C}$
 631 instead of $0.7 \text{ }^\circ\text{C}$ (see Eq. 4). This choice aims at reducing the sensitivity of EIS to atmospheric forcing in order to
 632 analyze whether the ice sheet is more responsive to the oceanic forcing.

633 Secondly, in EXP2, we found that increased precipitation as a result of increased temperatures (see Eq. 5) tends to
634 reduce the sensitivity of EIS. In the reference simulations (Section 4.2), the precipitation ratio to temperature
635 change (ω value) was set to $0.11\text{ }^{\circ}\text{C}^{-1}$. However, lower values can be found in the literature ranging between 0.05
636 $^{\circ}\text{C}^{-1}$ and $0.11\text{ }^{\circ}\text{C}^{-1}$ (Petrini et al., 2020, Charbit et al., 2013, Quiquet et al., 2013). We therefore investigated
637 whether the choice of a lower precipitation-temperature ratio, which is expected to lower the precipitation
638 dependency to temperatures, could influence the response of the EIS. In this new series of sensitivity experiments,
639 the ω parameter was fixed to $0.05\text{ }^{\circ}\text{C}^{-1}$. In doing so, our objective is to assess whether a variation in ω can lead to
640 significant changes in the response of the ice sheet to atmospheric forcing.

641 At last, Charbit et al. (2013) demonstrated that the choice of the PDD formulation can have a substantial
642 impact on the computed amount of ice melt. In order to assess the impact on the stability of the EIS of the melt
643 coefficient C_{ice} and C_{snow} , as defined in Tarasov and Peltier (2002), we decreased (resp. increased) their values
644 by 25% for the $+5^{\circ}\text{C}$ (resp. $+1^{\circ}\text{C}$) temperature perturbation. Decreasing (resp. increasing) the melt coefficients by
645 25% for the temperature perturbations allows to reduce (resp. increase) the influence of the atmospheric forcing
646 on the evolution of the EIS. In addition, in order to reduce the influence of the surface air temperatures, we have
647 also tested the impact of decreased melt coefficients in the basal melting perturbation experiments.

648 The results of these new sensitivity experiments are analyzed in terms of differences in ice volume loss at years
649 1000 and 10 000 years with the reference simulations (δ value, see Eq. 8) and are displayed in figure 11 (b-d). The
650 only significant differences with the reference simulations are obtained for a 5°C perturbation due to a lowered
651 temperature-elevation feedback in the simulation with $\lambda = 0.4\text{ }^{\circ}\text{C km}^{-1}$. For all the other experiments changes in
652 the ω parameter or in the degree-day factors, differences with reference simulations are less than $\pm 2\%$. As
653 such, this series of perturbed experiments shows that changing climate-related model parameters results in only
654 small changes in the EIS ice volume loss compared to the standard configuration of the GRISLI ice-sheet model,
655 and does not question the prevailing influence of the atmospheric forcing suggested by our reference sensitivity
656 experiments.

657 4.4.2 Sensitivity to physical parameterizations

658 Besides the climate related parameters, changes in the representation of the dynamic processes may have a strong
659 impact on the relative importance of the mechanisms responsible for the triggering of the EIS retreat. For example,
660 using the PSU ice sheet model (Pollard and De Conto, 2012), Petrini et al. (2018) found that the implementation
661 of a grounding line flux adjustment reduces the sensitivity of BKIS. To go a step further and compare our findings
662 with those of Petrini et al. (2018), we removed the grounding line flux parameterization in the GRISLI model and
663 assessed its impact on the EIS sensitivity. Without the flux adjustment, the EIS sensitivity to basal melting and
664 atmospheric temperature perturbations is reduced (Fig. 11e). This contrasts with the findings of Petrini et al (2018).
665 More specifically, after 10 000 years, a $+5^{\circ}\text{C}$ atmospheric perturbation results in a reduced amount of melting of
666 about 14% compared to the reference experiment (with parameterization of the grounding line flux). In other
667 words, these results suggest that in the absence of the grounding line flux adjustment, higher atmospheric
668 temperatures can potentially enhance the ice sheet's sensitivity to oceanic forcing through grounding line retreat.

669 Another source of huge uncertainties lies in the choice of the basal friction law (e.g. Brondex et al., 2017, Joughin
670 et al., 2019; Akesson et al., 2021). An appropriate choice of this law is of primary importance as basal friction

671 exerts a strong control on the dynamics of the grounding line and fast-flowing ice streams. In our previous
672 experiments, the basal friction was parameterized using a linear dragging law (Eq. 2). In order to investigate the
673 extent to which the choice of the friction law can influence the sensitivity of the EIS to atmospheric temperature
674 and basal melting perturbations we used a plastic dragging law where the basal drag depends quadratically on the
675 basal velocity (Pattyn et al., 2017).

676 In contrast to previous works investigating the ice sheet sensitivity to friction laws, our findings reveal that
677 experiments using the non-linear basal friction do not exhibit significant differences compared to EXP1 and EXP3
678 simulations after 1,000 and 10,000 years (Fig. 11f). However, it is important to note that Joughin et al. (2019) and
679 Akesson et al. (2021) explored the sensitivity of the Antarctic ice sheet, which differs from the EIS configuration.
680 This may explain (at least partly) why the EIS may exhibits a different sensitivity to changes in the friction law.

681 Thinning of confined ice shelves through basal melting produce a weakening of the buttressing effect, implying
682 an acceleration of the grounded ice streams and ultimately a substantial ice discharge in the ocean. This sequence
683 of events was observed in the Antarctic Peninsula after the collapse of the Larsen B Ice Shelf in 2002 (Rignot et
684 al., 2004; De Rydt et al., 2015). In our reference experiments, the ice shelf extent is small (Fig. 3). This likely
685 explains why the EIS appears poorly sensitive to basal melting. In order to potentially increase the area of ice
686 shelves, we reduced the calving criterion from 250 m to 50 m. This results in a slight increase of the ice shelf area
687 at the LGM (Fig. SP12d) compared to the reference simulations (Fig 3). However, this increase did not result in a
688 substantial change of the sensitivity of the EIS to basal melt and atmospheric temperature perturbations (Fig. 11 g).
689 This limitation is due to the topography, which does not allow for adequate confined ice shelf development, unlike
690 the Antarctic, where the presence of bays (in Ross and Weddell Seas for example) allows the formation of confined
691 ice shelves.

692 Thus; as previously highlighted for the GRISLI climate-related parameters, changing the parameterizations related
693 to ice dynamics does not modify the main conclusion related to the dominating effect of the atmospheric forcing
694 compared to the oceanic forcing.

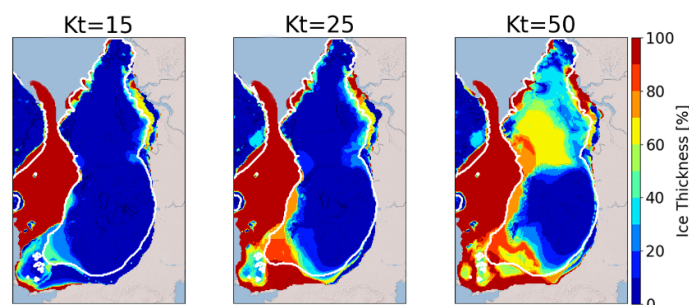
695 **5. Discussion**

696 The results of our experiments suggest that the EIS ice sheet is very sensitive to the atmospheric warming that may
697 have occurred at the beginning of the last deglaciation. By contrast, basal melting does not seem to be a key process
698 for triggering the ice sheet retreat. However, once the atmospheric warming has initiated the retreat, basal melting
699 has the capability of accelerating the retreat, as supported by the results of EXP4, providing that the amount of
700 basal melting is high enough. Nevertheless, these conclusions are strongly dependent on the ice-shelf
701 configurations. Indeed, unconfined ice shelves do not exert an efficient buttressing effect (i.e., the stress that the
702 ice shelves exert at the grounding line) and their removal has almost no impact on the dynamics of the grounded
703 ice sheet (Gundmundsson et al., 2013, Fürst et al., 2016).

704 The small sensitivity to the oceanic forcing simulated in the EXP3 experiments contradicts the conclusions of
705 previous modeling studies of the EIS behavior during the last glacial period (Alvarez-Solas et al., 2019) and the
706 last deglaciation (Petrini et al., 2020). Both conclude that oceanic temperatures are the main driver of the EIS
707 destabilization. Their findings are all the more surprising as they both use an ice-sheet model (GRISLI1.0) similar
708 to ours (GRISLI2.0). However, several differences can be noticed between their modeling approach and that of

709 the present study. First, GRISLI1.0 does not include a parameterization of the ice flux at the grounding line.
710 Therefore, it should be easier with our model to trigger the EIS retreat through basal melting because GRISLI2.0
711 includes key processes to simulate the marine ice sheet instability. To verify this issue, we performed additional
712 simulations similar to the EXP3 ones by removing the grounding line flux parameterization, and as expected,
713 results clearly show that the removal of this parameterization limits the ice loss (not shown). One of the most likely
714 explanation of the disagreement between our findings and those of previous studies (Alvarez-Solas et al., 2019;
715 Petrini et al., 2020) relies on the procedure followed in the spin-up experiments. Both built their initial state in the
716 same way. To favor the EIS build-up, they fixed the basal melting to 0.1 m yr^{-1} during their ice sheet spin-up.
717 Starting from the EIS configuration obtained at the end of the spin-up experiment, they used a linear (Alvarez-
718 Solas et al., 2019) or quadratic (Petrini et al., 2020) basal melting parameterization depending on the oceanic
719 temperature to simulate the last glacial period (Alvarez-Solas et al., 2019) or the last deglaciation (Petrini et al.,
720 2020) of EIS. In doing so, there is a methodological inconsistency between the spin-up simulation and the
721 subsequent experiments. To investigate the effect of such inconsistency on the EIS deglaciation, we followed their
722 spin-up methodology (homogeneous basal melting) instead of the one described in Section 2.3. The resulting LGM
723 ice sheets resemble those presented in Sec. 3.1, except that the MIROC-ESM forcing produces large ice shelves
724 in the Greenland and Norwegian seas. We then applied the same perturbations as in EXP3 on these alternative ice
725 sheets with a basal melting parameterization depending on the oceanic temperature and salinity (see Eq7). We
726 display in Figure 12 the percentage of ice thickness lost after 10000 years with respect to the initial configuration
727 for Kt ranging from 15 to $50 \text{ m } ^\circ\text{C}^{-1} \text{ yr}^{-1}$ for this new series of experiments. Compared to EXP3, we show that the
728 EIS now presents a much more significant sensitivity in the BIIS and FIS for a perturbation of $Kt=50 \text{ m } ^\circ\text{C}^{-1} \text{ yr}^{-1}$.
729 These results illustrate the extent to which the conclusions drawn for the driving mechanisms of the EIS
730 destabilization strongly depend on the initial state. However, we argue that the approach followed in the present
731 paper is more consistent as the basal melting parameterization is exactly the same for the spin-up procedure and
732 the sensitivity experiments.

733 Another difference that deserves to be mentioned is that Petrini et al, (2020) used a climatic index based on the
734 transient simulation of Liu et al., (2009). This method ensures that both the atmospheric and oceanic temperatures
735 increase concomitantly up to their pre-industrial levels. As a result, we cannot exclude that the key role of basal
736 melting in their simulated deglaciation is not amplified by the effect of atmospheric warming, similarly to the
737 conclusions drawn from our EXP4 results.



738
739 **Figure 12:** Multi-model mean of the ice thickness loss compared to the initial ice sheet for different basal melting
740 perturbations. LGM ice sheets are built by fixing the basal melting to 0.1 m yr^{-1} (as in Petrini et al., 2020; Alvarez-
741 Solas et al., 2019). Note that the significant decrease in ice thickness in the Norwegian and Greenland seas is due

742 to the simulation of ice shelves in the new spin-up for the MIROC-ESM forcing (see Fig. SP13). These ice shelves
743 are extremely sensitive to a change in the basal melt. The white line indicates the areas where the multi-model
744 mean is done on the 5 models.

745 The second round of sensitivity experiments conducted with new values of climate-related parameters and new
746 parameterizations related to the ice dynamics also confirm the high sensitivity of the EIS to the atmospheric forcing
747 in the GRISLI ice sheet model. This contrasts with the current situation in the West Antarctic Ice Sheet (WAIS),
748 where ice volume loss is mainly due to melting under the ice shelves (Pritchard et al., 2012). This difference in the
749 response of the two ice sheets raises questions about the mechanisms responsible for their respective evolution.

750 In addition, WAIS is characterized by large areas of confined ice shelves exerting a buttressing effect on the
751 grounded ice, whereas most of the ice shelves in our simulated LGM EIS are unconfined (see Section 4.4.2)
752 However, as temperatures are expected to rise in the future, larger amounts of meltwater will be produced on the
753 surface of the ice shelves (Kittel et al., 2021), favouring potentially the ice-shelf disintegration through
754 hydrofracturing (Banwell et al., 2013; Lai et al., 2020). Although this process differs from basal melting, it could
755 bring WAIS into a similar configuration to the past Eurasian ice sheet.

756 The ISMIP6 project (Seroussi et al., 2020) shows a significant difference in ice sheet behavior depending on the
757 ice sheet model used (Seroussi et al., 2020). Despite the numerous sensitivity experiments presented in this study
758 with various parameter values and different parameterizations of the ice dynamics (see section 4.4), we cannot
759 totally exclude the possible model-dependency of our results To reduce the uncertainties associated with the use
760 of a single ice sheet model, we strongly encourage other ice-sheet modelers to perform the same kind of sensitivity
761 tests with several other ice sheet models having, if possible, higher resolution so as to better capture the fine-scale
762 structure of outlet glaciers and the ice flow dynamics at the grounding line and the marine ice sheet instability.

763 **6. Conclusion**

764 In this paper, we used off-line GRISLI2.0 simulations forced by PMIP3/PMIP4 models to investigate the key
765 mechanisms driving the retreat of the Eurasian ice complex at the beginning of the last deglaciation. We gave a
766 special attention to the understanding of the processes responsible for the destabilization of the marine-based parts
767 of the Eurasian ice sheets as GRISLI2.0 includes an explicit calculation of the ice flux at the grounding line which
768 is expected to account for the representation of the marine ice sheet instability. We first showed that, due to too
769 strong climate biases in some GCMs at the LGM, only 5 out of 10 GCMs succeeded in building an ice sheet in
770 agreement with the reconstructions.

771 The sensitivity experiments have been designed to test the response of the simulated Eurasian ice sheets to surface
772 climate, oceanic temperature and sea level perturbations. Our results highlight the high EIS sensitivity to a change
773 in surface atmospheric temperatures using the GRISLI model. While basal melting does not seem to be the main
774 driver of the ice sheet retreat, we showed that its effect is clearly amplified by the atmospheric warming.

775 These results contradict those of previous studies mentioning the central role of the ocean on the deglaciation of
776 BKIS. However, we argue that parts of this disagreement are related to the way the climatic forcing is done
777 (absolute climatic fields, anomalies or climatic indexes) and the procedure followed for building the initial state
778 of EIS and to the presence of confined or unconfined ice shelves at the LGM. In order to assess the robustness of

779 our analyses, we suggest to other modelling groups to reproduce the same kind of sensitivity tests with ice sheet
780 models of similar or higher complexity. This pluralistic approach would allow to better understand the
781 uncertainties associated with the ice sheet model used.

782

783 **Data availability.** The source data of the experiments presented in the main text of the paper are available on the
784 Zenodo repository with the digital object identifier <https://doi.org/10.5281/zenodo.7528183> (van Aalderen et al,
785 2023).

786 **Code availability.** The GRISLI2.0 code is available upon request from Aurelien Quiquet
787 (aurelien.quiquet@lsce.ipsl.fr) and Christophe Dumas (christophe.dumas@lsce.ipsl.fr) (Laboratoire des Sciences
788 du Climat et de l'Environnement (LSCE)).

789 **Author contributions.** All authors designed the study. VVA performed the numerical experiments. All authors
790 contributed to the analysis of model results. VVA and SC wrote the manuscript with inputs from CD and AQ.

791 **Competing interests.** The authors declare that they have no conflict of interest

792 **Acknowledgements.** The authors are very grateful to Irina Rogozhina who edited the manuscript as well as two
793 anonymous reviewers for their constructive comments that greatly help improve the manuscript. Victor van
794 Aalderen is funded by the French National Research Agency (Grant: ANR-19-CE01-15). We acknowledge the
795 World Climate Research Programme's Working Group on Coupled Modelling, which is responsible for the
796 Paleoclimate Modelling Intercomparison Project (PMIP) and we thank the climate modeling groups (listed in
797 Table 1 of this paper) for producing and making available their model outputs. This work benefited from
798 productive exchanges with Nicolas Jourdain and Didier Swingedouw.

799

800

801

802

803

804

805

806

807

808

809

810

811 **References**

- 812 Abe-Ouchi, A., Saito, F., Kageyama, M., Braconnot, P., Harrison, S. P., Lambeck, K., Otto-Bliesner, B. L., Peltier,
813 W. R., Tarasov, L., Peterschmitt, J.-Y., and Takahashi, K.: Ice-sheet configuration in the CMIP5/PMIP3 Last
814 Glacial Maximum experiments, *Geosci. Model Dev.*, 8, 3621–3637, <https://doi.org/10.5194/gmd-8-3621-2015>,
815 2015.
- 816 Adloff, M., Reick, C. H., and Claussen, M.: Earth system model simulations show different feedback strengths of
817 the terrestrial carbon cycle under glacial and interglacial conditions, *Earth Syst. Dynam.*, 9, 413–425,
818 <https://doi.org/10.5194/esd-9-413-2018>, 2018.
- 819 Åkesson, H., Morlighem, M., O'Regan, M., and Jakobsson, M.: Future Projections of Petermann Glacier Under
820 Ocean Warming Depend Strongly on Friction Law, *JGR Earth Surface*, 126,
821 <https://doi.org/10.1029/2020JF005921>, 2021.
- 822 Alvarez-Solas, J., Banderas, R., Robinson, A., and Montoya, M.: Ocean-driven millennial-scale variability of the
823 Eurasian ice sheet during the last glacial period simulated with a hybrid ice-sheet–shelf model, *Clim. Past*, 15,
824 957–979, <https://doi.org/10.5194/cp-15-957-2019>, 2019.
- 825 Amante, C.: ETOPO1 1 Arc-Minute Global Relief Model: Procedures, Data Sources and Analysis,
826 <https://doi.org/10.7289/V5C8276M>, 2009.
- 827 Andreassen, K. and Winsborrow, M.: Signature of ice streaming in Bjørnøyrenna, Polar North Atlantic, through
828 the Pleistocene and implications for ice-stream dynamics, *Ann. Glaciol.*, 50, 17–26,
829 <https://doi.org/10.3189/172756409789624238>, 2009.
- 830 Annan, J. D., Hargreaves, J. C., and Mauritsen, T.: A new global surface temperature reconstruction for the Last
831 Glacial Maximum, *Clim. Past*, 18, 1883–1896, <https://doi.org/10.5194/cp-18-1883-2022>, 2022.
- 832 Banwell, A. F., MacAyeal, D. R., and Sergienko, O. V.: Breakup of the Larsen B Ice Shelf triggered by chain
833 reaction drainage of supraglacial lakes: LARSEN B CHAIN REACTION LAKE DRAINAGE, *Geophys. Res.*
834 *Let.*, 40, 5872–5876, <https://doi.org/10.1002/2013GL057694>, 2013.
- 835 Batchelor, C. L., Margold, M., Krapp, M., Murton, D. K., Dalton, A. S., Gibbard, P. L., Stokes, C. R., Murton, J.
836 B., and Manica, A.: The configuration of Northern Hemisphere ice sheets through the Quaternary, *Nat Commun*,
837 10, 3713, <https://doi.org/10.1038/s41467-019-11601-2>, 2019.
- 838 Beckmann, A. and Goosse, H.: A parameterization of ice shelf–ocean interaction for climate models, *Ocean*
839 *Modelling*, 5, 157–170, [https://doi.org/10.1016/S1463-5003\(02\)00019-7](https://doi.org/10.1016/S1463-5003(02)00019-7), 2003.
- 840 Beghin, P., Charbit, S., Dumas, C., Kageyama, M., Roche, D. M., and Ritz, C.: Interdependence of the growth of
841 the Northern Hemisphere ice sheets during the last glaciation: the role of atmospheric circulation, *Clim. Past*, 10,
842 345–358, <https://doi.org/10.5194/cp-10-345-2014>, 2014.
- 843 Briggs, R. D., Pollard, D., and Tarasov, L.: A data-constrained large ensemble analysis of Antarctic evolution
844 since the Eemian, *Quaternary Science Reviews*, 103, 91–115, <https://doi.org/10.1016/j.quascirev.2014.09.003>,
845 2014.
- 846 Brondex, J., Gagliardini, O., Gillet-Chaulet, F., and Durand, G.: Sensitivity of grounding line dynamics to the
847 choice of the friction law, *J. Glaciol.*, 63, 854–866, <https://doi.org/10.1017/jog.2017.51>, 2017.
- 848 Carlson, A. E. and Clark, P. U.: Ice sheet sources of sea level rise and freshwater discharge during the last
849 deglaciation, *Rev. Geophys.*, 50, RG4007, <https://doi.org/10.1029/2011RG000371>, 2012.
- 850 Colleoni, F., Masina, S., Cherchi, A., Navarra, A., Ritz, C., Peyaud, V., and Otto-Bliesner, B.: Modeling Northern
851 Hemisphere ice-sheet distribution during MIS 5 and MIS 7 glacial inception, *Clim. Past*, 10, 269–291,
852 <https://doi.org/10.5194/cp-10-269-2014>, 2014.
- 853 De Rydt, J., Gudmundsson, G. H., Rott, H., and Bamber, J. L.: Modeling the instantaneous response of glaciers
854 after the collapse of the Larsen B Ice Shelf: LARSEN B INSTANTANEOUS SPEEDUP, *Geophys. Res. Lett.*, 42,
855 5355–5363, <https://doi.org/10.1002/2015GL064355>, 2015.

856 Dowdeswell, J. A., Canals, M., Jakobsson, M., Todd, B. J., Dowdeswell, E. K., and Hogan, K. A.: The variety and
857 distribution of submarine glacial landforms and implications for ice-sheet reconstruction, *Memoirs*, 46, 519–552,
858 <https://doi.org/10.1144/M46.183>, 2016.

859 Dowdeswell, J. A., Montelli, A., Akhmanov, G., Solovyeva, M., Terekhina, Y., Mironyuk, S., and Tokarev, M.:
860 Late Weichselian ice-sheet flow directions in the Russian northern Barents Sea from high-resolution imagery of
861 submarine glacial landforms, *Geology*, 49, 1484–1488, <https://doi.org/10.1130/G49252.1>, 2021.

862 Dufresne, J.-L., Foujols, M.-A., Denvil, S., Caubel, A., Marti, O., Aumont, O., Balkanski, Y., Bekki, S., Bellenger,
863 H., Benshila, R., Bony, S., Bopp, L., Braconnot, P., Brockmann, P., Cadule, P., Cheruy, F., Codron, F., Cozic, A.,
864 Cugnet, D., de Noblet, N., Duvel, J.-P., Ethé, C., Fairhead, L., Fichefet, T., Flavoni, S., Friedlingstein, P.,
865 Grandpeix, J.-Y., Guez, L., Guilyardi, E., Hauglustaine, D., Hourdin, F., Idelkadi, A., Ghattas, J., Jousaume, S.,
866 Kageyama, M., Krinner, G., Labetoulle, S., Lahellec, A., Lefebvre, M.-P., Lefevre, F., Levy, C., Li, Z. X., Lloyd,
867 J., Lott, F., Madec, G., Mancip, M., Marchand, M., Masson, S., Meurdesoif, Y., Mignot, J., Musat, I., Parouty, S.,
868 Polcher, J., Rio, C., Schulz, M., Swingedouw, D., Szopa, S., Talandier, C., Terray, P., Viovy, N., and Vuichard,
869 N.: Climate change projections using the IPSL-CM5 Earth System Model: from CMIP3 to CMIP5, *Clim Dyn*, 40,
870 2123–2165, <https://doi.org/10.1007/s00382-012-1636-1>, 2013.

871 Durand, G., Gagliardini, O., de Fleurian, B., Zwinger, T., and Le Meur, E.: Marine ice sheet dynamics: Hysteresis
872 and neutral equilibrium, *J. Geophys. Res.*, 114, F03009, <https://doi.org/10.1029/2008JF001170>, 2009.

873 Eyring, V., Bony, S., Meehl, G. A., Senior, C. A., Stevens, B., Stouffer, R. J., and Taylor, K. E.: Overview of the
874 Coupled Model Intercomparison Project Phase 6 (CMIP6) experimental design and organization, *Geosci. Model*
875 *Dev.*, 9, 1937–1958, <https://doi.org/10.5194/gmd-9-1937-2016>, 2016.

876 Fürst, J. J., Durand, G., Gillet-Chaulet, F., Tavard, L., Rankl, M., Braun, M., and Gagliardini, O.: The safety band
877 of Antarctic ice shelves, *Nature Clim Change*, 6, 479–482, <https://doi.org/10.1038/nclimate2912>, 2016.

878 Gandy, N., Gregoire, L. J., Ely, J. C., Clark, C. D., Hodgson, D. M., Lee, V., Bradwell, T., and Ivanovic, R. F.:
879 Marine ice sheet instability and ice shelf buttressing of the Minch Ice Stream, northwest Scotland, *The Cryosphere*,
880 12, 3635–3651, <https://doi.org/10.5194/tc-12-3635-2018>, 2018.

881 Gandy, N., Gregoire, L. J., Ely, J. C., Cornford, S. L., Clark, C. D., and Hodgson, D. M.: Collapse of the Last
882 Eurasian Ice Sheet in the North Sea Modulated by Combined Processes of Ice Flow, Surface Melt, and Marine Ice
883 Sheet Instabilities, *J. Geophys. Res. Earth Surf.*, 126, <https://doi.org/10.1029/2020JF005755>, 2021.

884 Goelzer, H., Nowicki, S., Payne, A., Larour, E., Seroussi, H., Lipscomb, W. H., Gregory, J., Abe-Ouchi, A.,
885 Shepherd, A., Simon, E., Agosta, C., Alexander, P., Aschwanden, A., Barthel, A., Calov, R., Chambers, C., Choi,
886 Y., Cuzzone, J., Dumas, C., Edwards, T., Felikson, D., Fettweis, X., Golledge, N. R., Greve, R., Humbert, A.,
887 Huybrechts, P., Le clec'h, S., Lee, V., Leguy, G., Little, C., Lowry, D. P., Morlighem, M., Nias, I., Quiquet, A.,
888 Rückamp, M., Schlegel, N.-J., Slater, D. A., Smith, R. S., Straneo, F., Tarasov, L., van de Wal, R., and van den
889 Broeke, M.: The future sea-level contribution of the Greenland ice sheet: a multi-model ensemble study of ISMIP6,
890 *The Cryosphere*, 14, 3071–3096, <https://doi.org/10.5194/tc-14-3071-2020>, 2020.

891 Gowan, E. J., Zhang, X., Khosravi, S., Rovere, A., Stocchi, P., Hughes, A. L. C., Gyllencreutz, R., Mangerud, J.,
892 Svendsen, J.-I., and Lohmann, G.: A new global ice sheet reconstruction for the past 80 000 years, *Nat Commun*,
893 12, 1199, <https://doi.org/10.1038/s41467-021-21469-w>, 2021.

894 Gudlaugsson, E., Humbert, A., Andreassen, K., Clason, C. C., Kleiner, T., and Beyer, S.: Eurasian ice-sheet
895 dynamics and sensitivity to subglacial hydrology, *J. Glaciol.*, 63, 556–564, <https://doi.org/10.1017/jog.2017.21>,
896 2017.

897 Gudmundsson, G. H.: Ice-shelf buttressing and the stability of marine ice sheets, *The Cryosphere*, 7, 647–655,
898 <https://doi.org/10.5194/tc-7-647-2013>, 2013.

899 Hajima, T., Watanabe, M., Yamamoto, A., Tatebe, H., Noguchi, M. A., Abe, M., Ohgaito, R., Ito, A., Yamazaki,
900 D., Okajima, H., Ito, A., Takata, K., Ogochi, K., Watanabe, S., and Kawamiya, M.: Development of the MIROC-
901 ES2L Earth system model and the evaluation of biogeochemical processes and feedbacks, *Geosci. Model Dev.*,
902 13, 2197–2244, <https://doi.org/10.5194/gmd-13-2197-2020>, 2020.

- 903 Holland, P. R., Jenkins, A., and Holland, D. M.: The Response of Ice Shelf Basal Melting to Variations in Ocean
904 Temperature, *Journal of Climate*, 21, 2558–2572, <https://doi.org/10.1175/2007JCLI1909.1>, 2008.
- 905 Hughes, A. L. C., Gyllencreutz, R., Lohne, Ø. S., Mangerud, J., and Svendsen, J. I.: The last Eurasian ice sheets –
906 a chronological database and time-slice reconstruction, *DATED-1, Boreas*, 45, 1–45,
907 <https://doi.org/10.1111/bor.12142>, 2016.
- 908 Hutter, K.: The Response of a Glacier or an Ice Sheet to Seasonal and Climatic Changes, in: *Theoretical*
909 *Glaciology*, Springer Netherlands, Dordrecht, 333–423, https://doi.org/10.1007/978-94-015-1167-4_6, 1983.
- 910 Joughin, I., Smith, B. E., and Schoof, C. G.: Regularized Coulomb Friction Laws for Ice Sheet Sliding: Application
911 to Pine Island Glacier, Antarctica, *Geophysical Research Letters*, 46, 4764–4771,
912 <https://doi.org/10.1029/2019GL082526>, 2019.
- 913 Kageyama, M., Harrison, S. P., Kapsch, M.-L., Lofverstrom, M., Lora, J. M., Mikolajewicz, U., Sherriff-Tadano,
914 S., Vadsaria, T., Abe-Ouchi, A., Bouttes, N., Chandan, D., Gregoire, L. J., Ivanovic, R. F., Izumi, K., LeGrande,
915 A. N., Lhardy, F., Lohmann, G., Morozova, P. A., Ohgaito, R., Paul, A., Peltier, W. R., Poulsen, C. J., Quiquet,
916 A., Roche, D. M., Shi, X., Tierney, J. E., Valdes, P. J., Volodin, E., and Zhu, J.: The PMIP4 Last Glacial Maximum
917 experiments: preliminary results and comparison with the PMIP3 simulations, *Clim. Past*, 17, 1065–1089,
918 <https://doi.org/10.5194/cp-17-1065-2021>, 2021.
- 919 Kittel, C., Amory, C., Agosta, C., Jourdain, N. C., Hofer, S., Delhasse, A., Doutreloup, S., Huot, P.-V., Lang, C.,
920 Fichet, T., and Fettweis, X.: Diverging future surface mass balance between the Antarctic ice shelves and
921 grounded ice sheet, *The Cryosphere*, 15, 1215–1236, <https://doi.org/10.5194/tc-15-1215-2021>, 2021.
- 922 Konrad, H., Shepherd, A., Gilbert, L., Hogg, A. E., McMillan, M., Muir, A., and Slater, T.: Net retreat of Antarctic
923 glacier grounding lines, *Nature Geosci*, 11, 258–262, <https://doi.org/10.1038/s41561-018-0082-z>, 2018.
- 924 Ladant, J.-B., Donnadieu, Y., Lefebvre, V., and Dumas, C.: The respective role of atmospheric carbon dioxide and
925 orbital parameters on ice sheet evolution at the Eocene-Oligocene transition: Ice sheet evolution at the EOT,
926 *Paleoceanography*, 29, 810–823, <https://doi.org/10.1002/2013PA002593>, 2014.
- 927 Lai, C.-Y., Kingslake, J., Wearing, M. G., Chen, P.-H. C., Gentine, P., Li, H., Spergel, J. J., and van Wessem, J.
928 M.: Vulnerability of Antarctica’s ice shelves to meltwater-driven fracture, *Nature*, 584, 574–578,
929 <https://doi.org/10.1038/s41586-020-2627-8>, 2020.
- 930 Lambeck, K.: Late Devensian and Holocene shorelines of the British Isles and North Sea from models of glacio-
931 hydro-isostatic rebound, *JGS*, 152, 437–448, <https://doi.org/10.1144/gsjgs.152.3.0437>, 1995.
- 932 Lambeck, K.: Glaciation and sea-level change for Ireland and the Irish Sea since Late Devensian/Midlandian time,
933 *JGS*, 153, 853–872, <https://doi.org/10.1144/gsjgs.153.6.0853>, 1996.
- 934 Lambeck, K., Purcell, A., Zhao, J., and Svensson, N.-O.: The Scandinavian Ice Sheet: from MIS 4 to the end of
935 the Last Glacial Maximum, *Boreas*, 39, 410–435, <https://doi.org/10.1111/j.1502-3885.2010.00140.x>, 2010.
- 936 Lambeck, K., Rouby, H., Purcell, A., Sun, Y., and Sambridge, M.: Sea level and global ice volumes from the Last
937 Glacial Maximum to the Holocene, *Proc. Natl. Acad. Sci. U.S.A.*, 111, 15296–15303,
938 <https://doi.org/10.1073/pnas.1411762111>, 2014.
- 939 Le clec’h, S., Quiquet, A., Charbit, S., Dumas, C., Kageyama, M., and Ritz, C.: A rapidly converging initialisation
940 method to simulate the present-day Greenland ice sheet using the GRISLI ice sheet model (version 1.3), *Geosci.*
941 *Model Dev.*, 12, 2481–2499, <https://doi.org/10.5194/gmd-12-2481-2019>, 2019.
- 942 Le Meur, E. and Huybrechts, P.: A comparison of different ways of dealing with isostasy: examples from
943 modelling the Antarctic ice sheet during the last glacial cycle, *Ann. Glaciol.*, 23, 309–317,
944 <https://doi.org/10.3189/S0260305500013586>, 1996.
- 945 Liu, Z., Otto-Bliesner, B. L., He, F., Brady, E. C., Tomas, R., Clark, P. U., Carlson, A. E., Lynch-Stieglitz, J.,
946 Curry, W., Brook, E., Erickson, D., Jacob, R., Kutzbach, J., and Cheng, J.: Transient Simulation of Last
947 Deglaciation with a New Mechanism for Bølling-Allerød Warming, *Science*, 325, 310–314,
948 <https://doi.org/10.1126/science.1171041>, 2009.

- 949 MacAyeal, D. R.: Large-scale ice flow over a viscous basal sediment: Theory and application to ice stream B,
950 Antarctica, *J. Geophys. Res.*, 94, 4071–4087, <https://doi.org/10.1029/JB094iB04p04071>, 1989.
- 951 MARGO Project Members: Constraints on the magnitude and patterns of ocean cooling at the Last Glacial
952 Maximum, *Nature Geosci*, 2, 127–132, <https://doi.org/10.1038/ngeo411>, 2009a.
- 953 MARGO Project Members: Constraints on the magnitude and patterns of ocean cooling at the Last Glacial
954 Maximum, *Nature Geosci*, 2, 127–132, <https://doi.org/10.1038/ngeo411>, 2009b.
- 955 Marsh, O. J., Fricker, H. A., Siegfried, M. R., Christianson, K., Nicholls, K. W., Corr, H. F. J., and Catania, G.:
956 High basal melting forming a channel at the grounding line of Ross Ice Shelf, Antarctica, *Geophysical Research*
957 *Letters*, 43, 250–255, <https://doi.org/10.1002/2015GL066612>, 2016.
- 958 Marshall, S. J., Sharp, M. J., Burgess, D. O., and Anslow, F. S.: Near-surface-temperature lapse rates on the Prince
959 of Wales Icefield, Ellesmere Island, Canada: implications for regional downscaling of temperature, *Int. J.*
960 *Climatol.*, 27, 385–398, <https://doi.org/10.1002/joc.1396>, 2007.
- 961 Mauritsen, T., Bader, J., Becker, T., Behrens, J., Bittner, M., Brokopf, R., Brovkin, V., Claussen, M., Crueger, T.,
962 Esch, M., Fast, I., Fiedler, S., Fläschner, D., Gayler, V., Giorgetta, M., Goll, D. S., Haak, H., Hagemann, S.,
963 Hedemann, C., Hohenegger, C., Ilyina, T., Jahns, T., Jimenez-de-la-Cuesta, D., Jungclaus, J., Kleinen, T., Kloster,
964 S., Kracher, D., Kinne, S., Kleberg, D., Lasslop, G., Kornblueh, L., Marotzke, J., Matei, D., Meraner, K.,
965 Mikolajewicz, U., Modali, K., Möbis, B., Müller, W. A., Nabel, J. E. M. S., Nam, C. C. W., Notz, D., Nyawira,
966 S., Paulsen, H., Peters, K., Pincus, R., Pohlmann, H., Pongratz, J., Popp, M., Raddatz, T. J., Rast, S., Redler, R.,
967 Reick, C. H., Rohrschneider, T., Schemann, V., Schmidt, H., Schnur, R., Schulzweida, U., Six, K. D., Stein, L.,
968 Stemmler, I., Stevens, B., Storch, J., Tian, F., Voigt, A., Vrese, P., Wieners, K., Wilkenskjeld, S., Winkler, A., and
969 Roeckner, E.: Developments in the MPI-M Earth System Model version 1.2 (MPI-ESM1.2) and Its Response to
970 Increasing CO₂, *J. Adv. Model. Earth Syst.*, 11, 998–1038, <https://doi.org/10.1029/2018MS001400>, 2019.
- 971 Mercer, J. H.: Antarctic Ice and Interglacial High Sea Levels, *Science*, 168, 1605–1606,
972 <https://doi.org/10.1126/science.168.3939.1605.b>, 1970.
- 973 Mougnot, J., Rignot, E., and Scheuchl, B.: Continent-Wide, Interferometric SAR Phase, Mapping of Antarctic
974 Ice Velocity, *Geophysical Research Letters*, 46, 9710–9718, <https://doi.org/10.1029/2019GL083826>, 2019.
- 975 Nowicki, S., Goelzer, H., Seroussi, H., Payne, A. J., Lipscomb, W. H., Abe-Ouchi, A., Agosta, C., Alexander, P.,
976 Asay-Davis, X. S., Barthel, A., Bracegirdle, T. J., Cullather, R., Felikson, D., Fettweis, X., Gregory, J. M.,
977 Hattermann, T., Jourdain, N. C., Kuipers Munneke, P., Larour, E., Little, C. M., Morlighem, M., Nias, I., Shepherd,
978 A., Simon, E., Slater, D., Smith, R. S., Straneo, F., Trusel, L. D., van den Broeke, M. R., and van de Wal, R.:
979 Experimental protocol for sea level projections from ISMIP6 stand-alone ice sheet models, *The Cryosphere*, 14,
980 2331–2368, <https://doi.org/10.5194/tc-14-2331-2020>, 2020.
- 981 Patton, H., Hubbard, A., Andreassen, K., Auriac, A., Whitehouse, P. L., Stroeven, A. P., Shackleton, C.,
982 Winsborrow, M., Heyman, J., and Hall, A. M.: Deglaciation of the Eurasian ice sheet complex, *Quaternary Science*
983 *Reviews*, 169, 148–172, <https://doi.org/10.1016/j.quascirev.2017.05.019>, 2017.
- 984 Pattyn, F.: Sea-level response to melting of Antarctic ice shelves on multi-centennial timescales with the fast
985 Elementary Thermomechanical Ice Sheet model (f.ETISh v1.0), *The Cryosphere*, 11, 1851–1878,
986 <https://doi.org/10.5194/tc-11-1851-2017>, 2017.
- 987 Pattyn, F.: The paradigm shift in Antarctic ice sheet modelling, *Nat Commun*, 9, 2728,
988 <https://doi.org/10.1038/s41467-018-05003-z>, 2018.
- 989 Peltier, W. R.: On eustatic sea level history: Last Glacial Maximum to Holocene, *Quaternary Science Reviews*,
990 21, 377–396, [https://doi.org/10.1016/S0277-3791\(01\)00084-1](https://doi.org/10.1016/S0277-3791(01)00084-1), 2002.
- 991 Peltier, W. R., Argus, D. F., and Drummond, R.: Space geodesy constrains ice age terminal deglaciation: The
992 global ICE-6G_C (VM5a) model: Global Glacial Isostatic Adjustment, *J. Geophys. Res. Solid Earth*, 120, 450–
993 487, <https://doi.org/10.1002/2014JB011176>, 2015.

- 994 Petrini, M., Colleoni, F., Kirchner, N., Hughes, A. L. C., Camerlenghi, A., Rebesco, M., Lucchi, R. G., Forte, E.,
995 Colucci, R. R., and Noormets, R.: Interplay of grounding-line dynamics and sub-shelf melting during retreat of
996 the Bjørnøyrenna Ice Stream, *Sci Rep*, 8, 7196, <https://doi.org/10.1038/s41598-018-25664-6>, 2018.
- 997 Petrini, M., Colleoni, F., Kirchner, N., Hughes, A. L. C., Camerlenghi, A., Rebesco, M., Lucchi, R. G., Forte, E.,
998 Colucci, R. R., Noormets, R., and Mangerud, J.: Simulated last deglaciation of the Barents Sea Ice Sheet primarily
999 driven by oceanic conditions, *Quaternary Science Reviews*, 238, 106314,
1000 <https://doi.org/10.1016/j.quascirev.2020.106314>, 2020.
- 1001 Peyaud, V., Ritz, C., and Krinner, G.: Modelling the Early Weichselian Eurasian Ice Sheets: role of ice shelves
1002 and influence of ice-dammed lakes, *Clim. Past*, 3, 375–386, <https://doi.org/10.5194/cp-3-375-2007>, 2007.
- 1003 Pollard, D. and DeConto, R. M.: Modelling West Antarctic ice sheet growth and collapse through the past five
1004 million years, *Nature*, 458, 329–332, <https://doi.org/10.1038/nature07809>, 2009.
- 1005 Pollard, D. and DeConto, R. M.: Description of a hybrid ice sheet-shelf model, and application to Antarctica,
1006 *Geosci. Model Dev.*, 5, 1273–1295, <https://doi.org/10.5194/gmd-5-1273-2012>, 2012.
- 1007 Polyak, L., Forman, S. L., Herlihy, F. A., Ivanov, G., and Krinitsky, P.: Late Weichselian deglacial history of the
1008 Svyataya (Saint) Anna Trough, northern Kara Sea, Arctic Russia, *Marine Geology*, 143, 169–188,
1009 [https://doi.org/10.1016/S0025-3227\(97\)00096-0](https://doi.org/10.1016/S0025-3227(97)00096-0), 1997.
- 1010 Pritchard, H. D., Arthern, R. J., Vaughan, D. G., and Edwards, L. A.: Extensive dynamic thinning on the margins
1011 of the Greenland and Antarctic ice sheets, *Nature*, 461, 971–975, <https://doi.org/10.1038/nature08471>, 2009.
- 1012 Pritchard, H. D., Ligtenberg, S. R. M., Fricker, H. A., Vaughan, D. G., van den Broeke, M. R., and Padman, L.:
1013 Antarctic ice-sheet loss driven by basal melting of ice shelves, *Nature*, 484, 502–505,
1014 <https://doi.org/10.1038/nature10968>, 2012.
- 1015 Quiquet, A. and Dumas, C.: The GRISLI-LSCE contribution to the Ice Sheet Model Intercomparison Project for
1016 phase 6 of the Coupled Model Intercomparison Project (ISMIP6) – Part 1: Projections of the Greenland ice sheet
1017 evolution by the end of the 21st century, *The Cryosphere*, 15, 1015–1030, [https://doi.org/10.5194/tc-15-1015-](https://doi.org/10.5194/tc-15-1015-2021)
1018 [2021](https://doi.org/10.5194/tc-15-1015-2021), 2021a.
- 1019 Quiquet, A. and Dumas, C.: The GRISLI-LSCE contribution to the Ice Sheet Model Intercomparison Project for
1020 phase 6 of the Coupled Model Intercomparison Project (ISMIP6) – Part 2: Projections of the Antarctic ice sheet
1021 evolution by the end of the 21st century, *The Cryosphere*, 15, 1031–1052, [https://doi.org/10.5194/tc-15-1031-](https://doi.org/10.5194/tc-15-1031-2021)
1022 [2021](https://doi.org/10.5194/tc-15-1031-2021), 2021b.
- 1023 Quiquet, A., Ritz, C., Punge, H. J., and Salas y Mélia, D.: Greenland ice sheet contribution to sea level rise during
1024 the last interglacial period: a modelling study driven and constrained by ice core data, *Clim. Past*, 9, 353–366,
1025 <https://doi.org/10.5194/cp-9-353-2013>, 2013.
- 1026 Quiquet, A., Dumas, C., Ritz, C., Peyaud, V., and Roche, D. M.: The GRISLI ice sheet model (version 2.0):
1027 calibration and validation for multi-millennial changes of the Antarctic ice sheet, *Geosci. Model Dev.*, 11, 5003–
1028 5025, <https://doi.org/10.5194/gmd-11-5003-2018>, 2018.
- 1029 Quiquet, A., Roche, D. M., Dumas, C., Bouttes, N., and Lhardy, F.: Climate and ice sheet evolutions from the last
1030 glacial maximum to the pre-industrial period with an ice-sheet–climate coupled model, *Clim. Past*, 17, 2179–2199,
1031 <https://doi.org/10.5194/cp-17-2179-2021>, 2021.
- 1032 Rasmussen, T. L. and Thomsen, E.: Climate and ocean forcing of ice-sheet dynamics along the Svalbard-Barents
1033 Sea ice sheet during the deglaciation ~20,000–10,000 years BP, *Quaternary Science Advances*, 3, 100019,
1034 <https://doi.org/10.1016/j.qsa.2020.100019>, 2021.
- 1035 Rignot, E.: Accelerated ice discharge from the Antarctic Peninsula following the collapse of Larsen B ice shelf,
1036 *Geophys. Res. Lett.*, 31, L18401, <https://doi.org/10.1029/2004GL020697>, 2004.
- 1037 Rignot, E., Mouginot, J., Scheuchl, B., van den Broeke, M., van Wessem, M. J., and Morlighem, M.: Four decades
1038 of Antarctic Ice Sheet mass balance from 1979–2017, *Proc. Natl. Acad. Sci. U.S.A.*, 116, 1095–1103,
1039 <https://doi.org/10.1073/pnas.1812883116>, 2019.

- 1040 Ritz, C., Rommelaere, V., and Dumas, C.: Modeling the evolution of Antarctic ice sheet over the last 420,000
 1041 years: Implications for altitude changes in the Vostok region, *J. Geophys. Res.*, 106, 31943–31964,
 1042 <https://doi.org/10.1029/2001JD900232>, 2001.
- 1043 Schoof, C.: Marine ice sheet stability, *J. Fluid Mech.*, 698, 62–72, <https://doi.org/10.1017/jfm.2012.43>, 2012.
- 1044 Sejrup, H. P., Hafliðason, H., Aarseth, I., King, E., Forsberg, C. F., Long, D., and Rokoengen, K.: Late Weichselian
 1045 glaciation history of the northern North Sea, *Boreas*, 23, 1–13, [https://doi.org/10.1111/j.1502-](https://doi.org/10.1111/j.1502-3885.1994.tb00581.x)
 1046 [3885.1994.tb00581.x](https://doi.org/10.1111/j.1502-3885.1994.tb00581.x), 2008.
- 1047 Sejrup, H. P., Hjelstuen, B. O., Patton, H., Esteves, M., Winsborrow, M., Rasmussen, T. L., Andreassen, K., and
 1048 Hubbard, A.: The role of ocean and atmospheric dynamics in the marine-based collapse of the last Eurasian Ice
 1049 Sheet, *Commun Earth Environ*, 3, 119, <https://doi.org/10.1038/s43247-022-00447-0>, 2022.
- 1050 Sepulchre, P., Caubel, A., Ladant, J.-B., Bopp, L., Boucher, O., Braconnot, P., Brockmann, P., Cozic, A.,
 1051 Donnadieu, Y., Dufresne, J.-L., Estella-Perez, V., Ethé, C., Fluteau, F., Foujols, M.-A., Gastineau, G., Ghattas, J.,
 1052 Hauglustaine, D., Hourdin, F., Kageyama, M., Khodri, M., Marti, O., Meurdesoif, Y., Mignot, J., Sarr, A.-C.,
 1053 Servonnat, J., Swingedouw, D., Szopa, S., and Tardif, D.: IPSL-CM5A2 – an Earth system model designed for
 1054 multi-millennial climate simulations, *Geosci. Model Dev.*, 13, 3011–3053, [https://doi.org/10.5194/gmd-13-3011-](https://doi.org/10.5194/gmd-13-3011-2020)
 1055 [2020](https://doi.org/10.5194/gmd-13-3011-2020), 2020.
- 1056 Seroussi, H., Nowicki, S., Payne, A. J., Goelzer, H., Lipscomb, W. H., Abe-Ouchi, A., Agosta, C., Albrecht, T.,
 1057 Asay-Davis, X., Barthel, A., Calov, R., Cullather, R., Dumas, C., Galton-Fenzi, B. K., Gladstone, R., Golledge,
 1058 N. R., Gregory, J. M., Greve, R., Hattermann, T., Hoffman, M. J., Humbert, A., Huybrechts, P., Jourdain, N. C.,
 1059 Kleiner, T., Larour, E., Leguy, G. R., Lowry, D. P., Little, C. M., Morlighem, M., Pattyn, F., Pelle, T., Price, S.
 1060 F., Quiquet, A., Reese, R., Schlegel, N.-J., Shepherd, A., Simon, E., Smith, R. S., Straneo, F., Sun, S., Trusel, L.
 1061 D., Van Breedam, J., van de Wal, R. S. W., Winkelmann, R., Zhao, C., Zhang, T., and Zwinger, T.: ISMIP6
 1062 Antarctica: a multi-model ensemble of the Antarctic ice sheet evolution over the 21st century, *The Cryosphere*,
 1063 14, 3033–3070, <https://doi.org/10.5194/tc-14-3033-2020>, 2020.
- 1064 Shapiro, N.: Inferring surface heat flux distributions guided by a global seismic model: particular application to
 1065 Antarctica, *Earth and Planetary Science Letters*, 223, 213–224, <https://doi.org/10.1016/j.epsl.2004.04.011>, 2004.
- 1066 Solgaard, A., Kusk, A., Merryman Boncori, J. P., Dall, J., Mankoff, K. D., Ahlstrøm, A. P., Andersen, S. B.,
 1067 Citterio, M., Karlsson, N. B., Kjeldsen, K. K., Korsgaard, N. J., Larsen, S. H., and Fausto, R. S.: Greenland ice
 1068 velocity maps from the PROMICE project, *Earth Syst. Sci. Data*, 13, 3491–3512, [https://doi.org/10.5194/essd-13-](https://doi.org/10.5194/essd-13-3491-2021)
 1069 [3491-2021](https://doi.org/10.5194/essd-13-3491-2021), 2021.
- 1070 Stokes, C.: Palaeo-ice streams, *Quaternary Science Reviews*, 20, 1437–1457, [https://doi.org/10.1016/S0277-](https://doi.org/10.1016/S0277-3791(01)00003-8)
 1071 [3791\(01\)00003-8](https://doi.org/10.1016/S0277-3791(01)00003-8), 2001.
- 1072 Sueyoshi, T., Ohgaito, R., Yamamoto, A., Chikamoto, M. O., Hajima, T., Okajima, H., Yoshimori, M., Abe, M.,
 1073 O’ishi, R., Saito, F., Watanabe, S., Kawamiya, M., and Abe-Ouchi, A.: Set-up of the PMIP3 paleoclimate
 1074 experiments conducted using an Earth system model, MIROC-ESM, *Geosci. Model Dev.*, 6, 819–836,
 1075 <https://doi.org/10.5194/gmd-6-819-2013>, 2013.
- 1076 Svendsen, J. I., Alexanderson, H., Astakhov, V. I., Demidov, I., Dowdeswell, J. A., Funder, S., Gataullin, V.,
 1077 Henriksen, M., Hjort, C., Houmark-Nielsen, M., Hubberten, H. W., Ingólfsson, Ó., Jakobsson, M., Kjær, K. H.,
 1078 Larsen, E., Lokrantz, H., Lunkka, J. P., Lyså, A., Mangerud, J., Mantiouchkov, A., Murray, A., Möller, P., Niessen,
 1079 F., Nikolskaya, O., Polyak, L., Saarnisto, M., Siegert, C., Siegert, M. J., Spielhagen, R. F., and Stein, R.: Late
 1080 Quaternary ice sheet history of northern Eurasia, *Quaternary Science Reviews*, 23, 1229–1271,
 1081 <https://doi.org/10.1016/j.quascirev.2003.12.008>, 2004.
- 1082 Svendsen, J. I., Briner, J. P., Mangerud, J., and Young, N. E.: Early break-up of the Norwegian Channel Ice Stream
 1083 during the Last Glacial Maximum, *Quaternary Science Reviews*, 107, 231–242,
 1084 <https://doi.org/10.1016/j.quascirev.2014.11.001>, 2015.
- 1085 Szuman, I., Kalita, J. Z., Ewertowski, M. W., Clark, C. D., and Livingstone, S. J.: Dynamics of the last
 1086 Scandinavian Ice Sheet’s southernmost sector revealed by the pattern of ice streams, *Boreas*, 50, 764–780,
 1087 <https://doi.org/10.1111/bor.12512>, 2021.

- 1088 Tarasov, L. and Richard Peltier, W.: Greenland glacial history and local geodynamic consequences, *Geophysical*
1089 *Journal International*, 150, 198–229, <https://doi.org/10.1046/j.1365-246X.2002.01702.x>, 2002.
- 1090 Tarasov, L., Dyke, A. S., Neal, R. M., and Peltier, W. R.: A data-calibrated distribution of deglacial chronologies
1091 for the North American ice complex from glaciological modeling, *Earth and Planetary Science Letters*, 315–316,
1092 30–40, <https://doi.org/10.1016/j.epsl.2011.09.010>, 2012.
- 1093 Tierney, J. E., Zhu, J., King, J., Malevich, S. B., Hakim, G. J., and Poulsen, C. J.: Glacial cooling and climate
1094 sensitivity revisited, *Nature*, 584, 569–573, <https://doi.org/10.1038/s41586-020-2617-x>, 2020.
- 1095 Tsai, V. C. and Gudmundsson, G. H.: An improved model for tidally modulated grounding-line migration, *J.*
1096 *Glaciol.*, 61, 216–222, <https://doi.org/10.3189/2015JoG14J152>, 2015.
- 1097 Ullman, D. J., LeGrande, A. N., Carlson, A. E., Anslow, F. S., and Licciardi, J. M.: Assessing the impact of
1098 Laurentide Ice Sheet topography on glacial climate, *Clim. Past*, 10, 487–507, [https://doi.org/10.5194/cp-10-487-](https://doi.org/10.5194/cp-10-487-2014)
1099 [2014](https://doi.org/10.5194/cp-10-487-2014), 2014.
- 1100 Voldoire, A., Sanchez-Gomez, E., Salas y Méliá, D., Decharme, B., Cassou, C., Sénési, S., Valeke, S., Beau, I.,
1101 Alias, A., Chevallier, M., Déqué, M., Deshayes, J., Douville, H., Fernandez, E., Madec, G., Maisonnave, E.,
1102 Moine, M.-P., Planton, S., Saint-Martin, D., Szopa, S., Tyteca, S., Alkama, R., Belamari, S., Braun, A., Coquart,
1103 L., and Chauvin, F.: The CNRM-CM5.1 global climate model: description and basic evaluation, *Clim Dyn*, 40,
1104 2091–2121, <https://doi.org/10.1007/s00382-011-1259-y>, 2013.
- 1105 Weertman, J.: On the Sliding of Glaciers, *J. Glaciol.*, 3, 33–38, <https://doi.org/10.3189/S0022143000024709>,
1106 1957.
- 1107 Winkelmann, R., Martin, M. A., Haseloff, M., Albrecht, T., Bueler, E., Khroulev, C., and Levermann, A.: The
1108 Potsdam Parallel Ice Sheet Model (PISM-PIK) – Part 1: Model description, *The Cryosphere*, 5, 715–726,
1109 <https://doi.org/10.5194/tc-5-715-2011>, 2011.
- 1110 Yukimoto, S., Adachi, Y., Hosaka, M., Sakami, T., Yoshimura, H., Hirabara, M., Tanaka, T. Y., Shindo, E.,
1111 Tsujino, H., Deushi, M., Mizuta, R., Yabu, S., Obata, A., Nakano, H., Koshiro, T., Ose, T., and Kitoh, A.: A New
1112 Global Climate Model of the Meteorological Research Institute: MRI-CGCM3 —Model Description and Basic
1113 Performance—, *Journal of the Meteorological Society of Japan*, 90A, 23–64, <https://doi.org/10.2151/jmsj.2012->
1114 [A02](https://doi.org/10.2151/jmsj.2012-A02), 2012.
- 1115 Zheng, W. and Yu, Y.: Paleoclimate simulations of the mid-Holocene and last glacial maximum by FGOALS,
1116 *Adv. Atmos. Sci.*, 30, 684–698, <https://doi.org/10.1007/s00376-012-2177-6>, 2013.
- 1117 Zwally, H. J., Li, J., Robbins, J. W., Saba, J. L., Yi, D., and Brenner, A. C.: Mass gains of the Antarctic ice sheet
1118 exceed losses, *J. Glaciol.*, 61, 1019–1036, <https://doi.org/10.3189/2015JoG15J071>, 2015.